5

RECONFIGURABLE, TUNABLE, AND NONLINEAR ARTIFICIAL TRANSMISSION LINES

5.1 INTRODUCTION

In this chapter, some materials, components, and technologies to implement reconfigurable and tunable artificial transmission lines are briefly reviewed and some applications of these lines are highlighted. In the considered structures, tuning is achieved through electronic actuation where, typically, changes in a capacitance, or local changes in the permittivity of a dielectric layer, are generated by the actuated voltage or applied field. These tunable or reconfigurable structures operate in the lineal regime. Conversely, the final part of the chapter is devoted to the topic of nonlinear transmission lines (NLTLs), where nonlinearity and dispersion combined give rise to soliton wave propagation.

The topics covered in this chapter could be the subject of an extensive study. Indeed, there are several textbooks entirely focused on some of the technologies considered to implement tunable components. It is not the purpose of this chapter to make an in-depth study of such technologies, but to discuss some ideas for the implementation of tunable and reconfigurable transmission lines based on their use, and to point out some relevant applications.

5.2 MATERIALS, COMPONENTS, AND TECHNOLOGIES TO IMPLEMENT TUNABLE DEVICES

The tuning components, materials, or technologies that will be considered for the implementation of reconfigurable artificial transmission lines in the following section,

Artificial Transmission Lines for RF and Microwave Applications, First Edition. Ferran Martín.

are briefly analyzed in the present section. The tuning principles, as well as their advantages and limitations are highlighted.

5.2.1 Varactor Diodes, Schottky Diodes, PIN Diodes, and Heterostructure Barrier Varactors

Semiconductor diodes are electronic devices well known since long time ago and typically (although not exclusively) consisting of a PN junction [1]. Usually, these devices are used as rectifiers and switches in many electronic circuits such as AC–DC converters, voltage multipliers, envelope detectors, and so on. By applying a forward voltage, the diodes exhibit a small DC resistance and current flows across the diode terminals. Conversely, by applying a reverse bias, the diode does not allow a DC current flow. In the reverse-biased state, diodes behave as voltage-dependent capacitors since the depletion region width varies (increases) with the applied voltage. Generally, the width of the depletion region is proportional to the square root of the applied voltage.[1] Since the capacitance is inversely proportional to the depletion region width, it follows that the capacitance is inversely proportional to the square root of applied voltage. Therefore, reverse-biased diodes can be used as voltage-controlled capacitors, and can be applied in various electronic circuits, such as voltage-controlled oscillators (VCOs), tunable filters, and so on. They can also be used in nonlinear regime for the implementation of frequency multipliers and mixers, among other components.

In their use as voltage-controlled capacitors, it is important to enhance the dependence of the capacitance of the diode with the applied voltage. Specific diodes manufactured to exploit this effect are usually called varactor diodes, varicap diodes, or tuning diodes. A figure of merit of varactor diodes is the range of variability of the capacitance with the applied bias; whereas in ordinary diodes, the focus is to minimize such capacitance. Varactor diodes are low-cost components, commercially available in surface-mount technology (SMT). With their use, it is possible to achieve significant tuning ranges since there are available components from the main semiconductor providers exhibiting very wide capacitance spans.

It is also worth mentioning that there are specific diodes for fast switching speeds (Schottky diodes). Schottky diodes are based on a metal–semiconductor junction (where the semiconductor is typically n-type doped). Fast switching in such diodes is related to the fact that, as compared to ordinary diodes (where the switching mechanism involves the removal or injection of minority carriers at both sides of the junction by diffusion and recombination), Schottky diodes do not involve minority carriers. Schottky diodes are majority carrier semiconductor devices. Therefore, no slow recombination of n- and p-type minority carriers is involved in the switching process, and Schottky diodes can switch much faster than ordinary PN rectifier diodes.

Another type of diodes frequently used in RF/microwave applications are those consisting of a wide and slightly doped (almost intrinsic) semiconductor layer

[1] This dependence is analytically achieved by considering an abrupt PN junction. In a more realistic junction, the width of the depletion region is proportional to the m-root of the reverse voltage, with $2 < m < 3$ [1].

sandwiched between a p-type and an n-type semiconductor region. Such semiconductor devices, called PIN diodes, exhibit a high breakdown voltage and a low level of junction capacitance by virtue of the presence of the wide intrinsic (i-type) layer. The depleted region in PIN diodes extends almost entirely in the whole intrinsic region. Under forward bias, the carrier concentration in the intrinsic region is much higher than the intrinsic-level carrier concentration. Due to this high injection level, the electric field extends deeply (almost the entire length) into the region and helps in speeding up the transport of charge carriers from the P to the N region. This results in faster operation of the diode, making it a suitable device for high-frequency applications.

Let us finalize this subsection by dedicating few words to the heterostructure barrier varactor (HBV), proposed by Kollberg and Rydberg [2]. Such semiconductor device exhibits a voltage-controlled capacitance, similar to a varactor diode. However, unlike a varactor diode, the HBV exhibits an antisymmetric current–voltage relationship and a symmetric capacitance–voltage relationship (Fig. 5.1). The device can be either forward or reverse biased giving the same capacitance values (for the same magnitude of the applied bias), and the maximum capacitance is achieved in the absence of bias. Obviously, this symmetric capacitance–voltage characteristic can only be achieved if the structure is symmetric. Thus, instead of using a metal–semiconductor junction (providing a triangular-shaped band structure) or a PN junction, the HBV active region is made by sandwiching a wide band gap semiconductor layer between two semiconductor layers with lower band gap material. The resulting heterostructure acts as a potential (rectangular-shaped) barrier for electrons, avoiding the flow of DC current under moderate and low applied voltages (the current at high voltages is due to

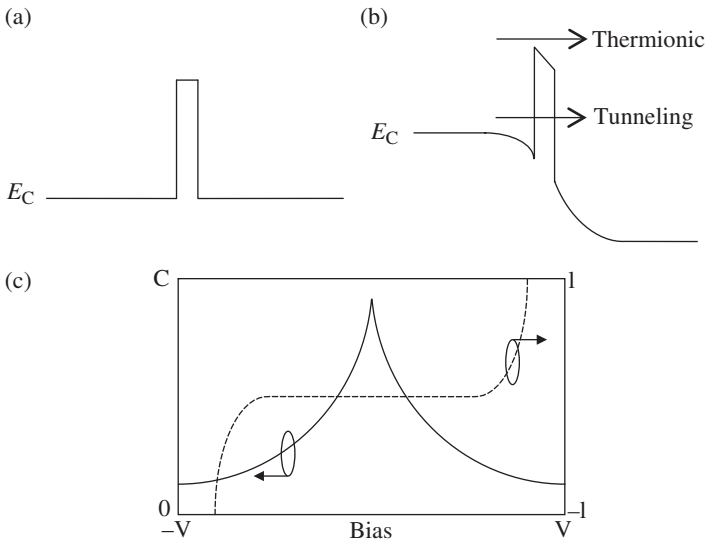

FIGURE 5.1 Conduction band diagram of an unbiased (a) and biased (b) HBV in the active (barrier) region, and typical capacitance–voltage and current–voltage diagrams (c). The current at high voltages may be due to thermionic emission or tunneling.

thermionic emission or tunneling). Basically, the barrier profile in equilibrium is symmetric around the middle of the barrier, and this symmetry is preserved if the heterostructure barrier is clad between two moderately doped semiconductor regions where the depleted region modulation takes place. Essentially, the structure exhibits a capacitive behavior where the extension of the depletion regions (essential to determine the voltage-dependent capacitance) is the same for forward and reverse conditions, and the capacitance–voltage characteristic is an even function. The symmetric capacitance–voltage characteristic of HBVs is not only of interest for biasing purposes in linear tunable components; several studies have also demonstrated the advantages of HBVs in nonlinear applications, particularly for efficiently rejecting the even-order harmonics in frequency multipliers [3] (this aspect will be considered in the last section of this chapter). In Section 5.3, the use of varactor diodes for the implementation of tunable metamaterial resonators and metamaterial transmission lines will be illustrated, and several examples of applications will be reported.

5.2.2 RF-MEMS

Microelectromechanical systems for radiofrequency applications (RF-MEMS) constitute a key enabling technology for telecommunication systems (see Ref. [4] and references therein). There are several areas where RF-MEMS may find application, but the focus here is the implementation of switches and variable capacitances for tunable/reconfigurable components. RF-MEMS can be classified depending on the actuation mechanism (electrostatic, thermal, magnetostatic, piezoelectric), configuration (fixed-fixed beam or cantilever beam type), and movement (continuous movement or switch), among others. The tunable/reconfigurable transmission lines and components that are described in the next section are based on electrostatically actuated RF-MEMS. Both configurations (fixed-fixed beam or cantilever) are considered, and RF-MEMS act as switchable components in most applications.

Figure 5.2 depicts the cross-sectional views of a nonactuated (up-state) and actuated (down-state) switchable cantilever type RF-MEMS. By application of a voltage, V,

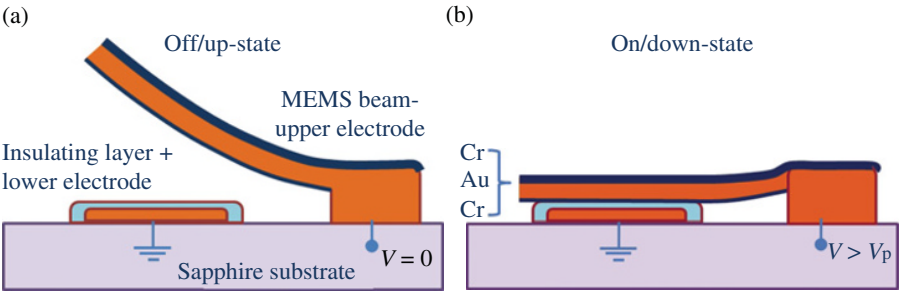

FIGURE 5.2 Cross sectional view of a cantilever-type beam RF-MEMS showing the two states: (a) nonactuated up-state and (b) actuated down-state when the applied voltage is higher than the MEMS pull-down voltage (V_p).

between the cantilever beam and the pull-down electrode, an electrostatic force is induced on the beam, and it deflects down as shown in Figure 5.2b. If the electrostatic force is larger than the mechanical restoring force, the switch stays in the down-state position. In order to estimate the required voltage to switch the RF-MEMS to the down-state, let us consider that the cantilever beam and the pull-down electrode are parallel oriented, so that their distance (beam height) is uniform in the whole area, regardless of the actuation voltage. Let us denote by g the distance between the beam and the pull-down electrode, g_o being the distance in the non-actuated state. The applied electrostatic force is given by

$$F_e = \frac{1}{2} V^2 \frac{dC(g)}{dg} \tag{5.1}$$

where the capacitance is[2]

$$C(g) = A\frac{\varepsilon_o}{g} \tag{5.2}$$

A being the effective area of the RF-MEMS capacitance. Equating the applied electrostatic force with the mechanical restoring force due to the stiffness of the beam, the following condition results [4]:

$$\frac{1}{2}\frac{\varepsilon_o A V^2}{g^2} = k(g_o - g) \tag{5.3}$$

where k is the spring constant. From (5.3), the necessary voltage to force a certain beam height, g, is

$$V = \sqrt{\frac{2kg^2(g_o - g)}{\varepsilon_o A}} \tag{5.4}$$

Notice that the right-hand side term in (5.4) exhibits a maximum for $g = (2/3)g_o$, and the corresponding voltage is

$$V_p = \sqrt{\frac{8kg_o^3}{27\varepsilon_o A}} \tag{5.5}$$

Thus, if the actuating voltage is $V > V_p$, there is not solution for (5.4), the system is unstable, and the beam and pull-down electrode collapse [4]. V_p is called pull-down voltage, and above that voltage the RF-MEMS is forced to be in the down-state. The

[2] Notice that the narrow insulating layer above the pull-down electrode has been neglected in the calculation of the capacitance $C(g)$.

instability is caused because for actuating voltages above V_p the restoring force is not able to compensate the electrostatic force. There is a positive feedback in the system, that is, as g decreases, the electrostatic force increases at a higher rate than the restoring force, and the beam finally collapses to the down-state. Cantilever beams generally exhibit smaller pull-down voltages, as compared to fixed-fixed beams, because they exhibit smaller spring constants [4].

In Section 5.3, several strategies to implement tunable metamaterial resonators using RF-MEMS are reported, including details relative to the fabrication process. As compared to varactor-based devices (useful for manufacturing tunable components in the L and S frequency bands), RF-MEMS can operate at much higher frequencies. Furthermore, the performance of varactor-based tunable microwave systems is generally limited by losses, power consumption, and nonlinearity. Conversely, the successful integration of RF-MEMS switches in electrically small metamaterial resonators is expected to be an enabling technology for many microwave applications (including the synthesis of metamaterial transmission lines and devices based on them), thanks to their low loss, near-zero power dissipation, compactness, high linearity on broad frequency bands, and very high capacitance ratios. RF-MEMS are still limited by reliability issues and moderate switching time, but progress has been done on these specific aspects [5–7]. The ability of this technology has been demonstrated over the past few years to provide an efficient solution to the tuning of microwave circuits [8, 9].

5.2.3 Ferroelectric Materials

Another possibility to implement tunable/reconfigurable RF/microwave components is to use materials with field-dependent constitutive parameters. Among them, ferroelectric materials are of special interest since they experience significant changes of the dielectric permittivity with an external electric field.[3] Hence, ferroelectric materials can be used for the implementation of variable capacitances, or as core substrates for the implementation of tunable resonators in planar technology [10].

Ferroelectric materials are able to exhibit spontaneous electric polarization in the absence of an external electric field (polar phase). Below the so-called Curie temperature, the spontaneous polarization can be reversed by an applied electric field, and the polarization is dependent not only on the instantaneous electric field but also on its history, yielding a hysteresis loop (materials exhibiting these properties are called ferroelectrics by analogy to ferromagnetic materials, which have spontaneous magnetization and also exhibit hysteresis loops). Above the Curie temperature, ferroelectric materials experience a phase transition, spontaneous polarization is not allowed, and they become paraelectric[4] (nonpolar phase). For microwave applications ferroelectric materials are typically used in the paraelectric phase since hysteresis is prevented [11]. This means that the operation temperature of the material must be above the

[3] The dielectric permittivity in ferroelectric materials also depends on temperature.

[4] Paraelectric materials exhibit a nonlinear dependence of the polarization with the electric field (or a field dependent permittivity).

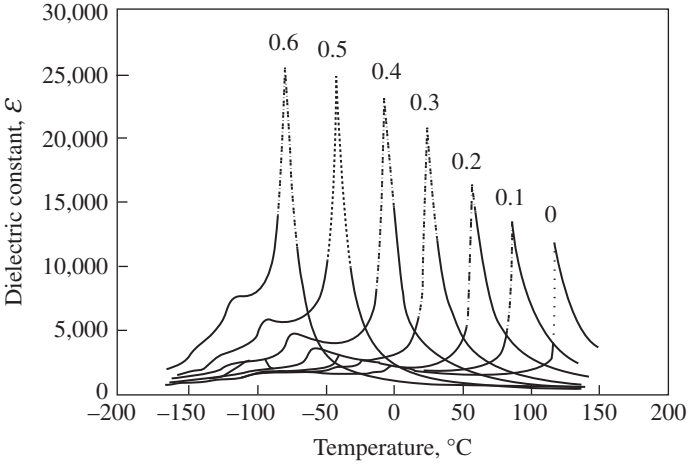

FIGURE 5.3 Dependence of the dielectric permittivity with temperature for several samples of BST with different values of the stoichiometic factor x. Reprinted with permission from Ref. [13]; copyright 2004 Elsevier.

Curie temperature. However, due to the fact that tunability (the variation of the permittivity with the external electric field) decreases as temperature increases from the Curie temperature, it is convenient to work just above the Curie point, where the permittivity reaches its maximum value [12]. Most ferroelectric materials are oxides with a perovskite crystalline structure, the most representative being the barium titanate ($BaTiO_3$). This material exhibits a Curie temperature of $T_c = 120°C$, that is, far above room temperature. Conversely, in strontium titanate ($SrTiO_3$) $T_c = -235°C$. This suggests that by combining such materials to form a mixed crystal of the type $Ba_xSr_{1-x}TiO_3$ (generally abbreviated as BST), the Curie temperature can be tailored with the stoichiometric factor x (see Fig. 5.3) [12, 13]. In particular, it has been found that for $x = 0.6$, the Curie temperature is $T_c = -2°C$. Therefore, $Ba_{0.6}Sr_{0.4}TiO_3$ exhibits paraelectric behavior at room temperature and is a good candidate material for the implementation of tunable components controlled by electric field.

BST exhibits high breakdown field strength (around 400 V/μm). This means that high biasing voltages can be applied for tuning, enhancing the achievable material tunability. Moreover, since the dielectric constant of BST can be set to various hundreds at room temperature,[5] film thicknesses as small as 2–6 μm are enough to implement tunable components. Typically thick (few microns) films of BST are screen printed on a carrier substrate (e.g., Al_2O_3) and the metallic layers are patterned on top of it. By virtue of the tunable permittivity of the BST layer, the capacitance between noncontacting (but closely separated) metallic strips (e.g., a capacitive gap) can be tailored by applying a voltage between the metallic terminals [14, 15]. This also applies to

[5] The dielectric permittivity is controlled by the stoichiometric factor x, but it is strongly influenced by the porosity of the BST material.

electrically small planar resonators, as will be discussed later. As compared to RF-MEMS, BST-based components are more robust, exhibit (in general) higher tunability ranges, but dielectric losses may limit device performance.

5.2.4 Liquid Crystals

Liquid crystals are a special class of materials that exhibit some properties of liquids and crystals simultaneously [16–18]. At the macroscopic level, liquid crystals behave like a liquid, being able to flow, move, and occupy arbitrarily shaped fixed volumes. At the microscopic level, liquid crystals have a rod-like molecule structure. Typically, the molecules are uniaxial, that is, they have one axis that is longer and preferred, with the other two being equivalent, but some liquid crystals are biaxial. The location of the particles is not fixed; but in the so-called nematic state, they are oriented along the main axis, maintaining long-range directional order (Fig. 5.4). Due to the high asymmetry of the liquid crystal molecules, the electromagnetic (EM) properties of these materials are expected to exhibit significant anisotropy. This is the case of the electric polarization, and the dielectric flux is related to the electric field by a permittivity tensor, rather than by a scalar. Nevertheless, if we consider the liquid crystal to be uniaxial, the permittivity tensor in the local molecule coordinate system (i.e., with axes parallel to the principal axes of the rod-shaped molecule) is diagonal, with parallel (to the main axis) and perpendicular (orthogonal to the main axis) permittivity denoted by $\varepsilon_{r\parallel}$ and $\varepsilon_{r\perp}$, respectively.

For tuning purposes in microwave circuits, nematic liquid crystals with controllable orientation of their molecules are of interest. Due to the anisotropy, the effective permittivity can be tuned by manipulating such orientation. In practice, the alignment of the main axis is usually achieved by application of a static electric or magnetic field.

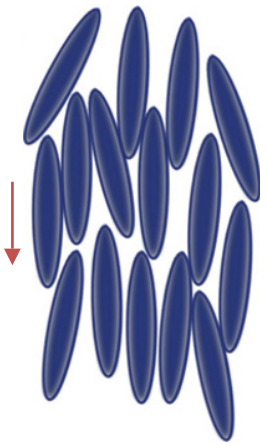

FIGURE 5.4 Scheme of the liquid crystal molecules in the nematic phase. The molecules do not necessarily all point in the same direction; however, the average of all the directors points in one direction (indicated).

Thus, in tunable microwave devices based on nematic liquid crystals, anisotropy plays a fundamental role and the tuning principle is completely different than those tuning principles studied in the previous subsections.

Liquid crystals typically exhibit small losses (at least as compared to ferroelectric materials), although the fact that they can flow makes the design/fabrication of liquid crystal-based devices more cumbersome (i.e., proper sealing is necessary). Other general advantages are high-frequency operation (up to hundreds of GHz), large tuning ranges, and fast switching times. This performance justifies the use of liquid crystals (despite the confinement requirements) in certain applications where these excellent properties must be satisfied simultaneously. Ignoring the inherent limitation (from the fabrication viewpoint) of dealing with a liquid, it is difficult to find a technology/material able to compete with liquid crystals for tuning purposes.

5.3 TUNABLE AND RECONFIGURABLE METAMATERIAL TRANSMISSION LINES AND APPLICATIONS

Several strategies for the implementation of tunable and reconfigurable metamaterial transmission lines, using the tunable components and materials presented in the previous section, are discussed in this section. The first part of the section is devoted to the implementation and applications of tunable lines based on SRRs and other related resonators. The second part focuses on the CL-loaded approach.

5.3.1 Tunable Resonant-Type Metamaterial Transmission Lines

The tuning principle in most metamaterial transmission lines implemented by means of split rings is based on the variation of the resonance frequency of the resonant elements through electronic actuation. This tuning can be achieved by loading the split rings (SRRs, OCSRRs, etc.,) with varactor diodes (or by means of other tuning diodes) or RF-MEMS. Alternatively, tunable resonant-type metamaterial transmission lines can be implemented by etching the resonant elements on top of tunable materials, such as ferroelectrics. Let us now discuss different approaches for the implementation of tunable split rings.

5.3.1.1 Varactor-Loaded Split Rings and Applications Probably, the simplest form to tune the resonance frequency of an SRR is by loading it with a voltage-controlled capacitor [19–21]. In practice, these capacitances can be implemented by means of tuning diodes, such as varactor diodes. The first SRR loaded with a varactor diode, designated as varactor-loaded split-ring resonator (VLSRR), was reported in Ref. [19]. The topology of that VLSRR [19] is depicted in Figure 5.5a. As compared to the SRR topology originally proposed by Pendry [22], the VLSRR reported in Ref. [19] was rectangular shaped, with a nonuniform distance d between the inner and outer ring, in order to accommodate the diode varactor between such rings. Moreover, a metal pad was added in the center of the particle to ease diode biasing. With this configuration, the EM behavior of the VLSRR does

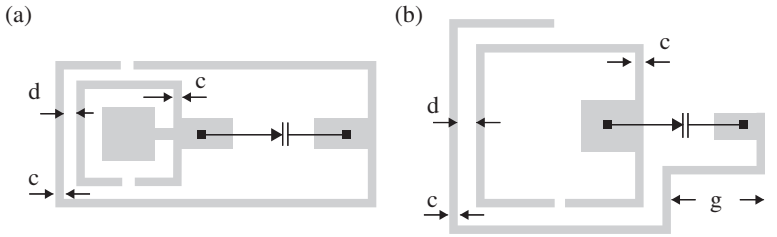

FIGURE 5.5 Topologies of the tunable VLSRR (a) and VLSRR with improved geometry (b). The relevant dimensions are indicated. Reprinted with permission from Ref. [20]; copyright 2006 IEEE.

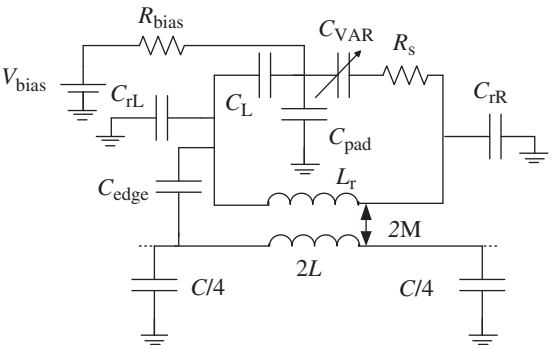

FIGURE 5.6 Lumped-element equivalent circuit model for the elemental cell of a biased VLSRR coupled to a microstrip transmission line. L and C are the per-section inductance and capacitance of the line. The magnetic wall concept has been used. Reprinted with permission from Ref. [20]; copyright 2006 IEEE.

not substantially differ from that of the SRR, except by the fact that the resonance frequency of the VLSRR can be tuned by virtue of the presence of the diode varactor (such varactor dominates over the edge capacitance of the right half of the structure). Due to the presence of the inner metallic pad, it is expected that particle excitation is mainly achieved through the magnetic field penetrating the inter-rings region, where the varactor is allocated, rather than by the axial magnetic field present within the inner ring of the particle (as in ordinary SRRs). An alternative, and simple, topology of the VLSRR is the one depicted in Figure 5.5b [20], where the right-hand arm of the outer ring has been shortened since no appreciable current flows through it (i.e., most of the electric current is absorbed by the varactor diode), and the metallic pad for diode soldering and polarization has been reduced. The result is a topology similar to that of a square-shaped SRR.

The lumped-element equivalent circuit model of a biased VLSRR coupled to a microstrip transmission line is depicted in Figure 5.6 [20]. The diode varactor is modeled by a variable capacitance, C_{VAR}, and a series resistance, R_s, which takes

into account not only the intrinsic losses of the diode, R_D, but also the resistance associated to the varactor–metal junctions, R_{VM}. C_R (which is neglected due to the shunt connection of C_{VAR} to it) and C_L are the edge capacitances corresponding to the right and left halves, respectively, of the VLSRR, whilst L_r and C_{pad} model the equivalent inductance of the VLSRRs and the pad-to-ground capacitance, respectively. Diode biasing is applied through a variable voltage source, V_{bias}, which has an equivalent output resistance termed R_{bias}. Concerning line-to-VLSRRs coupling, we a priori assume that VLSRRs can be driven either by the axial magnetic field generated by the line (inductive coupling) or by the electric field present between the line and the external ring (capacitive coupling). Both couplings have been properly modeled by means of a mutual inductance, M, (magnetic coupling) and the edge capacitance between the line and the external ring, C_{edge} (electric coupling). The capacitances C_{rL} and C_{rR} are the rings-to-ground capacitances of the left and right halves, respectively.

The VLSRR model of Figure 5.6 is validated by comparing the frequency response of a fabricated two-stage VLSRR-loaded microstrip line with the frequency response obtained through circuit simulation of the corresponding two-stage equivalent circuit of the VLSRR-loaded line. The fabricated device is depicted in Figure 5.7a, where *BB833-Infineon Technologies* silicon tuning diodes have been used as nonlinear capacitances (the capacitance window for these diodes is 0.75–9 pF for varying voltages in the interval 0–30 V). The device, fabricated on the *Rogers RO3010* substrate with dielectric constant $\varepsilon_r = 10.2$, thickness $h = 1.27$ mm and $\tan\delta = 0.0023$, exhibits stopband functionality, similar to SRR-loaded lines and attributed to the negative effective permeability of the structure in the vicinity of the fundamental resonance. However, due to the presence of varactors, the central frequency can be electronically tuned (Fig. 5.7b). Except the mutual inductance, M, and the varactor–metal junction resistance, R_{VM}, which have been used as fitting parameters, the other element values have been estimated either through geometrical considerations or with the help of the commercial software *Agilent ADS* (see Ref. [20] for details). The frequency responses depicted in Figure 5.7c have been obtained by setting $M = 1.2$ nH and $R_{VM} = 3\ \Omega$ (the other parameters are indicated in the caption of Fig. 5.7), and are those that have optimally fitted to the experiment over the considered tuning interval. The good agreement between theory and experiment supports the validity of the model. Nevertheless, the model can be simplified since no appreciable differences in the circuit simulation result by switching the electric coupling off (this can be simply achieved by removing the coupling capacitance, C_{edge}, and the capacitance C_{pad}, as Fig. 5.8a illustrates). The circuit simulations considering only inductive coupling as the single driving mechanism of the VLSRRs (Fig. 5.8a) are depicted in Figure 5.8b. The fact that the frequency responses for the different diode polarizations are very similar to those depicted in Figure 5.7b and c points out that magnetic coupling is the dominant coupling mechanism. According to this model, signal can flow through the resistance R_{bias}. However, since C_{rL} and C_{rR} are small, it is a good approximation, in order to simplify the analysis of the circuit, to neglect these capacitances and consider R_{bias} as a polarization path for the diodes (i.e., irrelevant for signal analysis). With this approximation, the equivalent impedance of the series branch of the transmission-line section

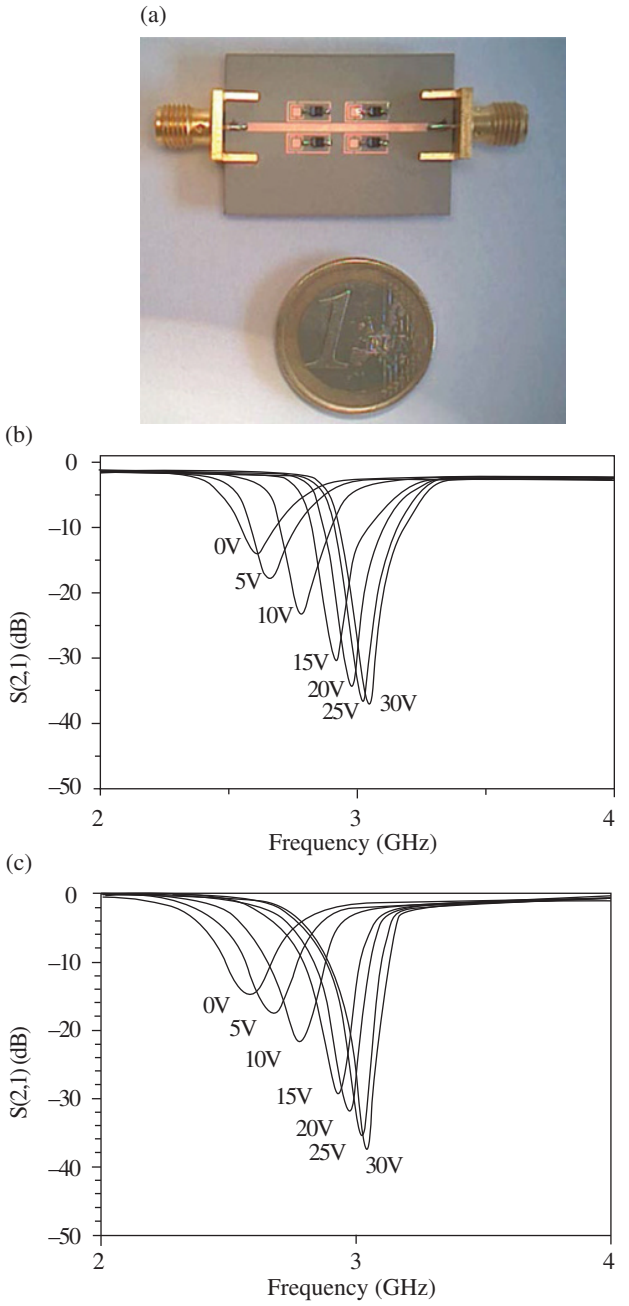

FIGURE 5.7 Photograph of a two-stage VLSRR-loaded microstrip line (a), measured insertion losses for different diode polarizations (b) and frequency responses obtained by circuit simulation of the equivalent circuit model shown in Fig. 5.6 (c). Relevant dimensions are $c = d = 0.2$ mm, separation between line and external rings is 0.2 mm and length and width of VLSRRs are 6.2 mm and 2.8 mm, respectively. Element values are $L_r = 3$ nH, $C_L = 1.4$ pF, $C_{edge} = 1$ fF, $C_{rL} = 0.1$ pF, $C_{pad} = 0.44$ pF, $C_{rR} = 0.89$ pF, $L = 3.3$ nH, $C = 1.3$ pF, $R_S = 4.8\ \Omega$, (i.e., $R_D = 1.8\ \Omega$ and $R_{VM} = 3.0\ \Omega$), $R_{bias} = 50\ \Omega$, $M = 1.2$ nH, and $1\text{ pF} \le C_{VAR} \le 9$ pF. Reprinted with permission from Ref. [20]; copyright 2006 IEEE.

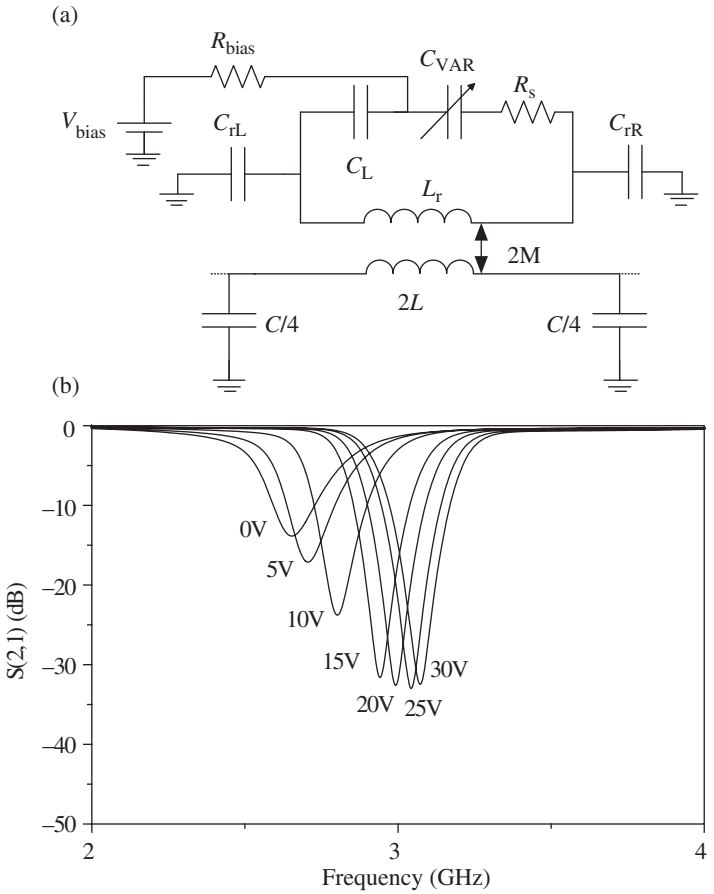

FIGURE 5.8 Equivalent circuit model of the VLSRR-loaded microstrip line with electric coupling removed (a), and circuit simulations for different diode polarizations (b). Reprinted with permission from Ref. [20]; copyright 2006 IEEE.

(including the effects of the resistance R_s) can be inferred. The result is the series connection of an inductor (with inductance $L' = 2L - L_s'$) and a parallel RLC tank, with element values given by[6]

$$L_s' = 4M^2 C_{eq} \omega_o^2 \tag{5.6a}$$

[6] These expressions are derived by applying the transformer equations to the circuit of Figure 5.8a with the approximations cited in the text. Notice also that L', L_s', and C_s' are identical to the expressions given in Figure 3.34, which are valid for a line loaded with SRRs only (i.e., without shunt-inductive elements).

$$C_s' = \frac{L_r}{4M^2\omega_o^2} \tag{5.6b}$$

$$R' = \frac{4M^2\omega_o^2}{R_s} \tag{5.6c}$$

where $\omega_o = (L_r C_{eq})^{-1/2}$. Expressions (5.6) explain the reduction in gap width and rejection enhancement when ω_o increases. Namely, the Q-factor of the RLC tank described by the elements of (5.6) is

$$Q = \omega_o R' C_s' = \omega_o \frac{L_r}{R_s} \tag{5.7}$$

and it increases with ω_o (R_s and L_r do not depend on frequency). Therefore, deeper and narrower stopbands are expected in the upper extreme of the tuning interval, as actually occurs. The agreement between measurements and circuit simulations of the equivalent-circuit model is good over the whole tuning interval. Therefore, the proposed equivalent-circuit model provides a good description of the VLSRR-loaded microstrip line.

Microstrip lines loaded with VLSRRs can be useful as tunable and reconfigurable stopband filters. It is possible to tune the filter central frequency and/or the filter bandwidth. As an illustrative example, Figure 5.9 depicts a four-stage stopband filter, where the VLSRR stages are all identical. By applying the same bias to the diodes, the central frequency is tuned (the bandwidth is slightly tuned as well, for the reasons explained before), as depicted in Figure 5.9b. However, we can also apply different bias voltages to the diodes in order to enhance filter bandwidth, as illustrated in Figure 5.9c.

By adding vias (acting as shunt connected inductors) or capacitive gaps (acting as series capacitors) to the VLSRR-loaded microstrip lines, the stopband is switched to a pass band [20]. Despite the fact that a tunable bandpass filter with roughly constant characteristics in the tuning interval was reported in Ref. [20] by adding gaps to the line, losses were found to be significant for most practical applications. To synthesize tunable bandpass filters with good performance, low-loss tuning elements, such as RF-MEMS, are necessary (the combination of RF-MEMS and SRRs, and their application to bandpass and bandstop filters, is discussed later).

CSRRs can also be combined with varactor diodes for the implementation of tunable components. The particle, first reported in Ref. [23], was called varactor-loaded complementary split-ring resonator (VLCSRR). Although CSRRs and SRRs are dual particles, the extension of the VLSRR concept to the VLCSRR is not obvious. The topology of the VLCSRR coupled to a microstrip transmission line, proposed in Ref. [23], is depicted in Figure 5.10. It consists of a CSRR etched in the ground plane, beneath the conductor strip, a varactor diode (with a variable capacitance C_{var}) and a lumped capacitance (C_L). The varactor diode and the lumped capacitance are series connected, and this combination is placed between the internal and external metallic

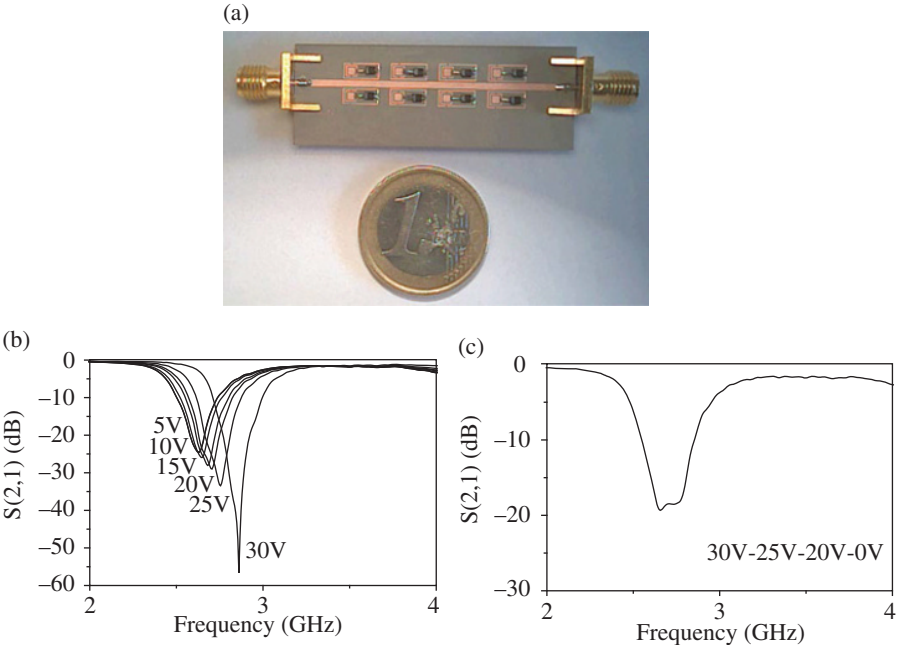

FIGURE 5.9 Fabricated four-stage VLSRR-loaded microstrip line (a), measured frequency response for identical bias voltages applied to the diode varactors (b), and measured transmission characteristics by applying the indicated voltages to the different VLSRR stages (c). Dimensions are identical to those of Figure 5.7a. Reprinted with permission from Ref. [20]; copyright 2006 IEEE.

regions of the CSRR, as can be seen in Figure 5.10. Actually, the varactor diode is soldered in the upper substrate side (see Fig. 5.10b), whereas the lumped capacitor is placed at the lower substrate side. The presence of the two indicated vias allows for the aforementioned configuration. Since the lumped-element equivalent circuit model of the CSRR is a parallel resonant tank, by adding a varactor diode between the internal and external metallic regions of the CSRR, the equivalent capacitance of the structure can be tuned. In practice, this can be achieved by placing the varactor diode on the top substrate side and connection to the bottom side through metallic vias. However, this is not so simple since the varactor diode must be biased and both diode ports are electrically connected with this arrangement. To solve this problem, the via 2 has been surrounded by a slot in the ground plane and a lumped capacitance has been placed between the ground plane and the via, as Figure 5.10a illustrates. It is clear that C_{var} and C_L are series connected. Since the equivalent capacitance of this combination is dominated by the smaller capacitance, it is convenient that C_L is at least of the same order than the maximum achievable capacitance of the varactor diode. According to these comments, the equivalent circuit model of the VLCSRR electrically coupled to the microstrip line is the one depicted in Figure 5.11, where

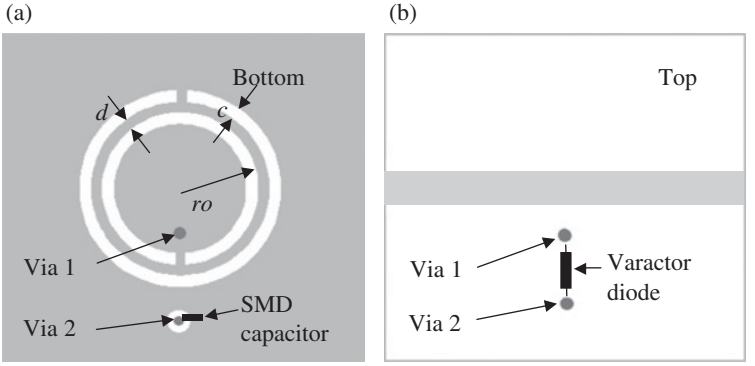

FIGURE 5.10 Topology of VLCSRR and relevant dimensions (a) bottom view and (b) top view. Reprinted with permission from Ref. [23]; copyright 2008 IEEE.

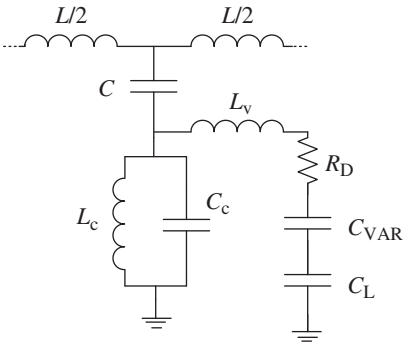

FIGURE 5.11 Lumped-element equivalent circuit model of the unit cell of a microstrip line loaded with VLCSRRs.

L_c and C_c are the inductance and capacitance of the CSRR, C is the coupling capacitance between the line and the VLCSRR, L is the line inductance, L_v is the inductance of the vias and R_D accounts for varactor losses. According to this model, to achieve significant tuning it is necessary that C_{var} dominates over C_c.

As it is, the structure of Figure 5.10 is expected to exhibit a stopband with tuning capability. This stopband is related to the presence of a transmission zero, f_z, (corresponding to that frequency that nulls the shunt reactance), where rejection is maximum. For a homogeneous structure comprising multiple unit cells, the stopband can also be interpreted as due to the high effective permittivity of the structure in the vicinity of the transmission zero, this being positive to the left of f_z and negative between f_z and the resonance frequency of the VLCSRRs.

The circuit model of Figure 5.11 is validated by comparing experimental data and circuit simulations. The fabricated device is a two-stage VLCSRR-loaded line (see Fig. 5.12) implemented on the *Rogers RO3010* substrate with thickness $h = 1.27$ mm

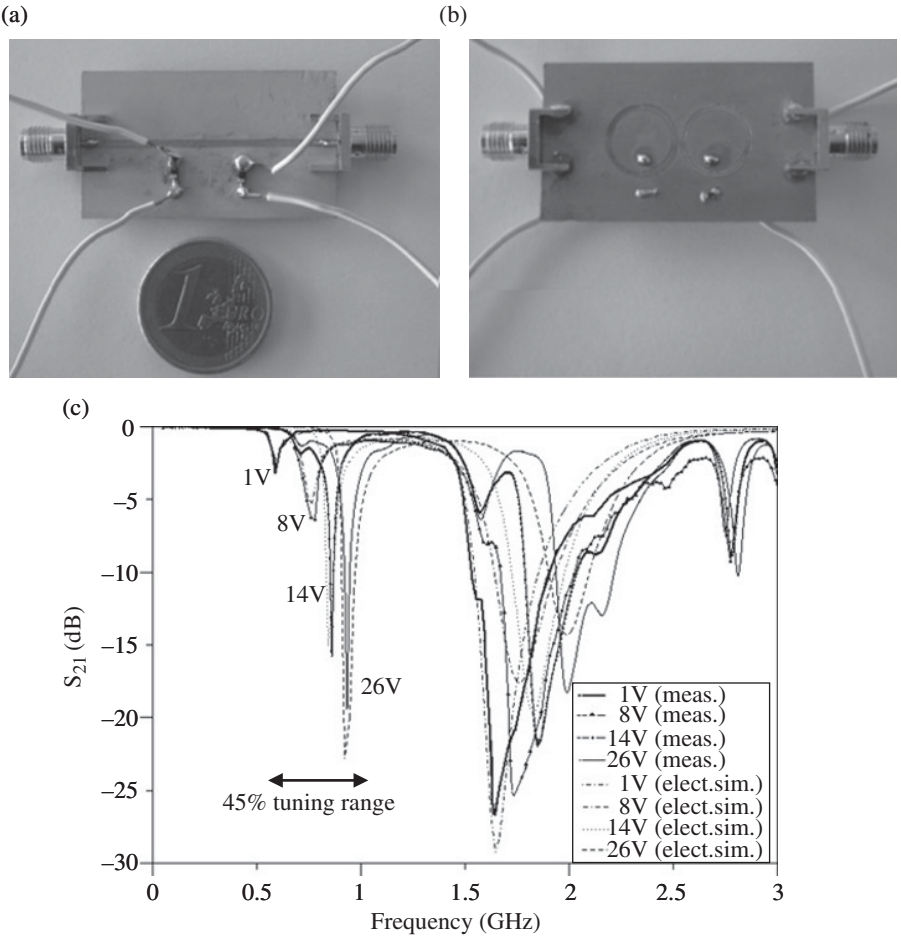

FIGURE 5.12 Photograph of the fabricated two-stage VLCSRR-loaded microstrip line. (a) Top view, (b) bottom view, and (c) measured and circuit simulation of the insertion loss for different bias polarizations. The region of interest is comprised between 0.5 GHz and 1 GHz, but the frequency response has been depicted up to 3 GHz to appreciate the validity of the model beyond that region. Circuit parameters are $L = 7.2$ nH, $C = 1.9$ pF, $C_c = 40$ pF, $L_c = 3.8$ nH, $R_D = 5.2\,\Omega$, and $L_v = 2.6$ nH. Reprinted with permission from Ref. [23]; copyright 2008 IEEE.

and dielectric constant $\varepsilon_r = 10.2$. In reference to Figure 5.10, dimensions are $c = 0.3$ mm, $d = 0.18$ mm and $r_o = 5.2$ mm. The diameter of the vias is 0.2 mm. The host line is a 50 Ω line with a width of 1.15 mm. The diode varactors are the *BB535-Infineon Technologies* silicon tuning diodes. These devices exhibit a high capacitance ratio, namely, device capacitance is 20 pF and 2.1 pF at 1 V and 28 V reverse bias, respectively. Finally, 4.7 pF SMD-type lumped capacitances have been used for C_L. The measured transmission coefficients corresponding to different bias voltages are

depicted in Figure 5.12b. Except for C_{var}, C_L, L_v, and R_D, the parameter values of the circuit model have been inferred from the parameter extraction method reported in Ref. [24], and presented in Appendix G. Such parameters have been obtained from the structures without the presence of the diode varactors and lumped capacitors and are indicated in the caption of Figure 5.12. The resistance R_D and the inductance of the vias L_v have been considered as fitting parameters. The best fit has been obtained by setting R_D and L_v to the values also indicated in the caption of Figure 5.12. The good agreement between the experimental curves and the circuit simulation in Figure 5.12c is remarkable. Notice that in the region of interest the tuning modifies the filter response, providing smaller rejection level as the central frequency decreases (a phenomenology similar to that of VLSRR-loaded lines).

By adding series capacitive gaps or shunt-inductive vias to the structure of Figure 5.10, the stopband behavior can be switched to a pass band. This possibility was demonstrated in Ref. [23], where a single cell VLCSRR-loaded line with a gap etched in the signal strip was fabricated and modeled by simply adding series capacitances to the line inductance, L, in the circuit of Figure 5.11. Although the agreement between the measured responses, for different voltages applied to the varactor, and the circuit simulations was found to be good, losses are important for using the structure as a tunable bandpass filter. This limitative aspect, related to diode losses, is identical to the encountered limitations of VLSRRs as tuning elements for bandpass filters (as indicated before). According to these comments and the results of this subsection, it is clear that VLSRR- and VLCSRR-loaded transmission lines exhibit very similar behavior.

The open counterparts of SRRs and CSRRs can also be combined with diode varactors for the implementation of tunable components [25]. Let us discuss the strategies for diode biasing in varactor-loaded open split-ring resonators (VLOSRRs) and varactor-loaded open complementary split-ring resonators (VLOCSRRs) in CPW technology. The VLOSRR is considered to be in shunt connection to the line (useful for the implementation of stopband filters [25]). The VLOCSRR, also in shunt connection, is useful for the implementation of tunable bandpass filters.

The typical topology of a shunt connected VLOSRR is depicted in Figure 5.13. The external ring is electrically connected to the central strip of the CPW transmission line, whereas the internal ring is electrically connected to ground. The varactor diode is connected between the inner ring and the metallic pad etched in the ground plane window close to the external ring. Diode polarization is achieved by applying a DC voltage to the metallic pad (in reference to the ground plane). To effectively short the upper pin of the diode to the external ring at the signal frequency, a large capacitance is required. This capacitance blocks the DC voltage, but acts as a bypass capacitor at microwave frequencies. Thus, with this topology we can electrically tune the resonance frequency of the shunt element. The equivalent circuit of the structure can be approximated by the model depicted in Figure 5.13b, where L and C are roughly the inductance and capacitance of the open split-ring resonator, and C_{VAR} is the variable capacitance of the varactor diode.

The typical topology of a shunt-connected VLOCSRR is depicted in Figure 5.14. In this case, the different metal regions of the structure are electrically shorted (similar

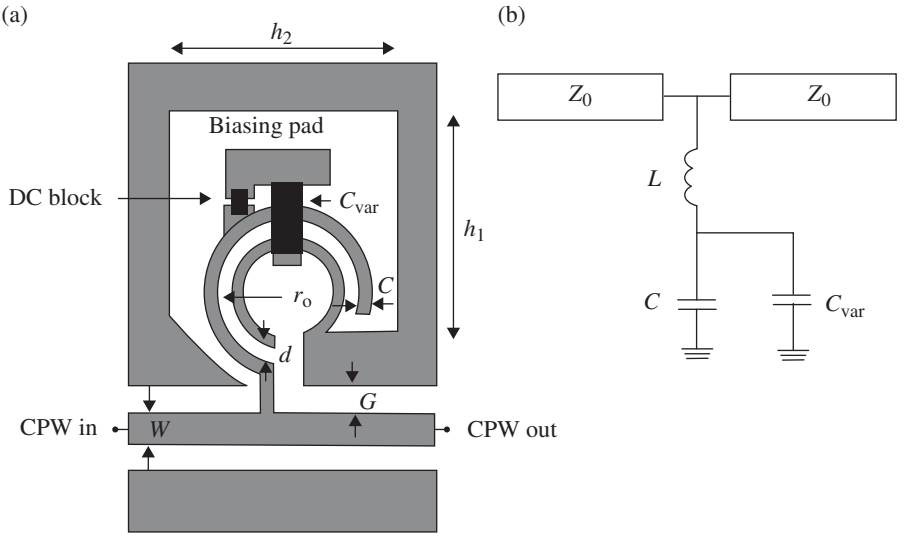

FIGURE 5.13 Typical layout of a shunt-connected VLOSRR in a CPW transmission line (a), and circuit model (b). Only one half of the CPW structure is shown. Reprinted with permission from Ref. [25]; copyright 2011 IET.

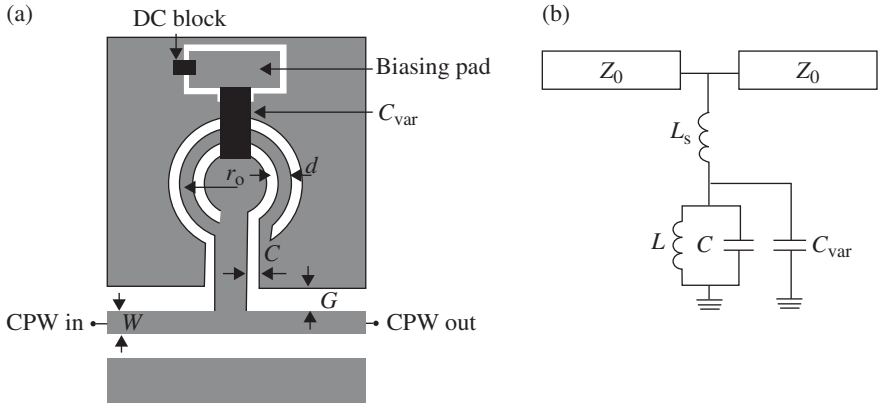

FIGURE 5.14 Typical layout of a shunt-connected VLOCSRR in a CPW transmission line (a) and circuit model (b). Only one half of the CPW structure is shown. Reprinted with permission from Ref. [25]; copyright 2011 IET.

to VLCSRRs). For this reason, we must etch an isolated bias pad, as shown in Figure 5.14. The varactor diode is soldered between the inner metallic region of the resonator and the bias pad. Again, a bypass capacitor is required in order to short the bias pad to the ground plane at microwave frequencies. The equivalent circuit model of the structure is that shown in Figure 5.14b, where L and C are roughly

the inductance and capacitance of the open complementary split-ring resonator, C_{VAR} is the variable capacitance of the varactor diode and L_s represents the inductive strip between the resonator and the central line of the CPW.

Both equivalent circuit models are validated by comparison of the EM response (actually the co-simulated electric and EM response) and the electrical (circuit) response for different voltage levels applied to the diode varactor. The co-simulations can be inferred by means of the *Agilent Momemtum* EM simulator. To this end, the EM responses of the structures, by considering internal ports in those positions where the lumped elements are connected, are obtained. Then, these results are exported to the circuit simulator, and the lumped components (i.e., the capacitances of the varactors at the considered voltages) are added to get the final results. In practice, these co-simulations were carried out by considering commercial diode model libraries (those of the *Infineon BB833* varactor diodes) and different applied voltages. The circuit simulations were obtained by means of the circuit simulator included in *Agilent ADS*. This comparison is presented in Figures 5.15 and 5.16 for a CPW structure loaded with a single VLOSRR and VLOCSRR, respectively, and shows the excellent accuracy of the model to describe the behavior of the tunable cells (this good agreement is relevant for the design and characterization of tunable filters). For the structure of Figure 5.13, applied voltages between 0 V and 28 V were considered, corresponding to varactor capacitance values of 9.3 pF and 0.75 pF, respectively, for the used varactors (Fig. 5.15 depicts the responses for the indicated voltages). The inductance L and capacitance C of the circuit model (Fig. 5.13b) were inferred by curve fitting, with the result of $L = 6.3$ nH and $C = 0.75$ pF. These values are of the same order than

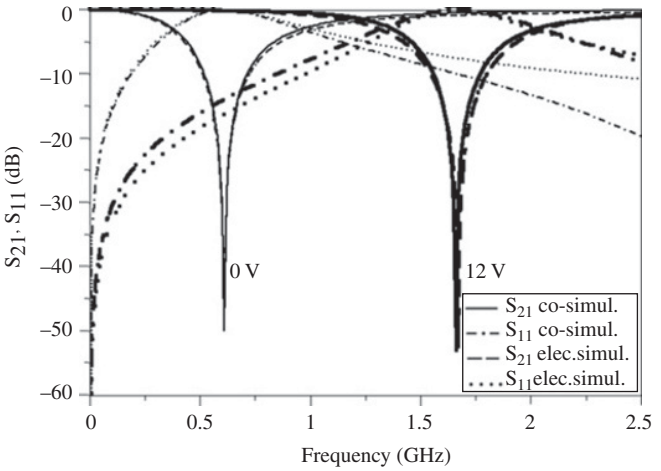

FIGURE 5.15 Comparison between circuit simulation and co-simulation (EM-electric) for different voltages applied to the VLOSRR of Figure 5.13. Dimensions (in reference to Fig. 5.13) are $W = 2.1$ mm, $G = 0.7$ mm, $r_0 = 2.29$ mm, $c = d = 0.38$ mm, $h_1 = 6.14$ mm, and $h_2 = 5.9$ mm. The circuit elements are $L = 6.3$ nH and $C = 0.75$ nH. Reprinted with permission from Ref. [25]; copyright 2011 IET.

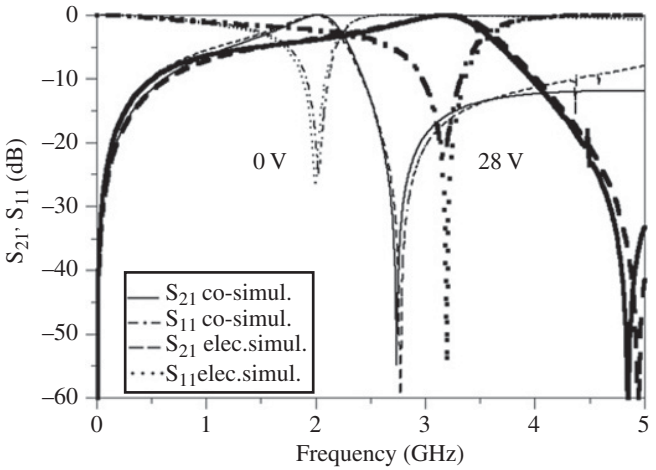

FIGURE 5.16 Comparison between circuit simulation and co-simulation (EM-electric) for different voltages applied to the VLOCSRR of Figure 5.14. Dimensions (in reference to Fig. 5.14) are $W = 1.68$ mm, $G = 3.7$ mm, $r_0 = 1.7$ mm, and $c = d = 0.3$ mm. The circuit elements are $L = 3.8$ nH, $C = 1.25$ nH and $L_s = 0.7$ nH. Reprinted with permission from Ref. [25]; copyright 2011 IET.

the values of capacitance and inductance of the isolated OSRR. For the structure of Figure 5.14, the same applied voltages were considered. The resulting circuit elements (of the circuit model of Fig. 5.14b), inferred by curve fitting, are in this case $L = 3.8$ nH, $C = 1.25$ pF and $L_s = 0.7$ nH.

Using the previous VLOSRRs- and VLOCSRR-loaded CPWs, tunable stopband and bandpass filters can be implemented. In this case, the filters were designed/implemented by coupling the resonators by means of admittance inverters [25], following the well-known approach reported in many textbooks devoted to microwave filters [26], and applied to the design of non-tunable bandpass and bandstop filters based on these open resonators [27, 28]. Notice, however, that tuning the resonance frequency of the particles would require tuning also the phase of the transmission line sections present between adjacent resonators, in order to achieve the admittance inversion functionality at the (tunable) filter central frequency. This strategy would require additional tuning elements and was discarded in the implementations reported in Ref. [25]. The designed tunable bandstop and bandpass filters, based on VLOSRRs and VLOCSRRs, respectively, are depicted in Figures 5.17 and 5.18, respectively (see Ref. [25] for further design details). The devices were fabricated on the *Rogers RO3010* substrate with dielectric constant $\varepsilon_r = 10.2$, thickness $h = 1.27$ mm and loss tangent $\tan\delta = 0.0023$. Relevant device dimensions are indicated in the caption of those figures. The tuning elements are the *Infineon BB833* varactor diodes (with a capacitance varying in the range 9.3–0.75 pF for voltages between 1 V and 28 V), and the bypass capacitors are the SMD *Phycom* capacitances with a value of 50 pF.

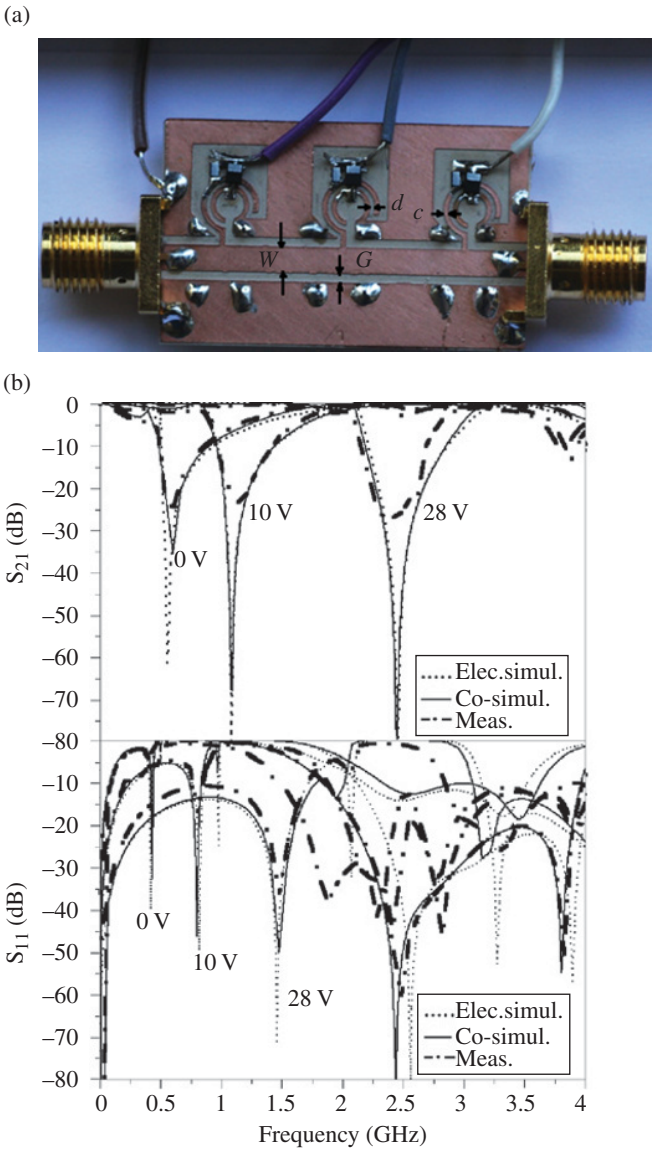

FIGURE 5.17 Photograph of the fabricated tunable band-stop filter (a) and comparison between co-simulated, pure electrically simulated and measured frequency responses for different applied voltages (b). Dimensions are $W = 2.1$ mm, $G = 0.7$ mm, $r_0 = 2.29$ mm, $c = d = 0.38$ mm, $h_1 = 6.14$ mm, and $h_2 = 5.9$ mm, and total device length is $l = 23$ mm. The different ground plane regions have been electrically connected through backside strips and vias to avoid the slot mode of the CPW structure. Reprinted with permission from Ref. [25]; copyright 2011 IET.

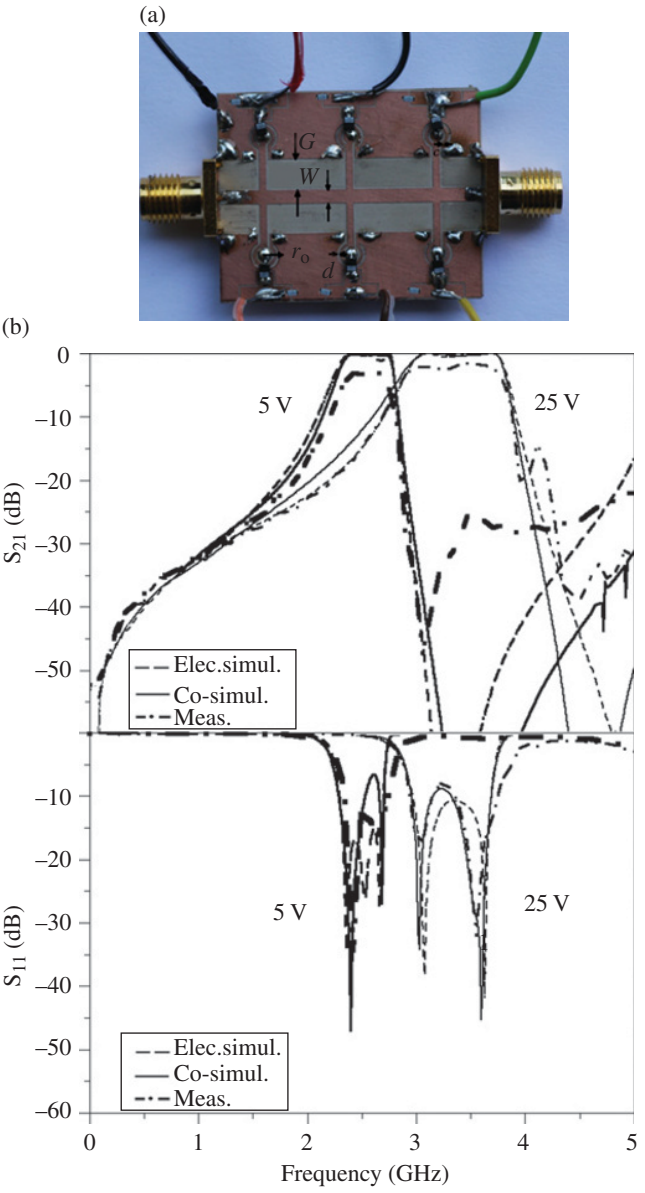

FIGURE 5.18 Photograph of the fabricated tunable bandpass filter (a) and comparison between co-simulated, pure electrically simulated and measured frequency response for different applied voltages (b). Dimensions are $W = 1.68$ mm, $G = 3.7$ mm, $r_0 = 1.7$ mm, $c = d = 0.3$ mm, and total device length is $l = 32$ mm. The different ground plane regions have been electrically connected through backside strips and vias to avoid the slot mode of the CPW structure. Reprinted with permission from Ref. [25]; copyright 2011 IET.

Prior to fabrication, the frequency response of the filters at different applied voltages was inferred from co-simulations (electric and EM). The results of the co-simulations (at different applied voltages) of the whole structures are also depicted in Figures 5.17 and 5.18 for the tunable stopband and bandpass filters, respectively. The pure electrical (circuit) simulations are also depicted in Figures 5.17 and 5.18, together with the measured frequency responses of the fabricated filters. The good agreement between the circuit simulations, the co-simulations and the measurements is remarkable, and further supports the validity of the reported models. The higher tuning range for the bandstop filter (as compared to that of the bandpass filter) is simply because the tunable capacitance clearly dominates over the resonator's capacitance in the considered OSRRs. In the OCSRRs of the band-pass filters, the tunable capacitance and resonator's capacitance are comparable and the tuning range is smaller. For the bandpass filter, in-band losses are present, but this level of losses may be acceptable for a tunable bandpass filter. Notice, however, that bandwidth is not controlled with the reported approach, and it decreases as the central frequency decreases, as Figure 5.18 illustrates.

Other tunable components based on varactor-loaded split rings have been reported. For instance, a tunable 1:2 power divider based on a VLCSRR-loaded line acting as impedance inverter (with 35.35 Ω impedance) is reported in Ref. [29]. To achieve the inverter functionality over the tuning interval, the structure is implemented with two additional tuning elements, acting as series connected variable capacitances. By this means, the line impedance and phase (90°) can be controlled over the tuning interval (nevertheless, the design procedure is complex and the author suggests paper [29] to the interested reader).

5.3.1.2 Tunable SRRs and CSRRs Based on RF-MEMS and Applications As anticipated in Section 5.2.2, RF-MEMS are very interesting components to implement tunable and reconfigurable split rings. As compared to varactor diodes, RF-MEMS can operate at higher frequencies and exhibit smaller levels of losses. The use of RF-MEMS for the implementation of tunable SRR-based metamaterials was reported in several papers (see, e.g., Refs [30, 31]). The purpose here is the implementation of transmission lines loaded with RF-MEMS-based tunable split rings. To this end, two main strategies have been considered: (1) split rings with RF-MEMS loading, where tuning is achieved through electrostatic actuation on a set of MEMS switches loading the resonators [32, 33], and (2) cantilever-type SRRs, where the arms of the SRR are deflectable [34]. Let us now discuss the principles behind these approaches, and some applications to tunable filters.

Split Rings with RF-MEMS Loading Concerning the first approach, both SRR [33] and CSRRs [32] loaded with RF-MEMS switches have been implemented. SRR tunability can be achieved by adding cantilever-type RF-MEMS switches, which are composed of one anchor and one movable beam suspended above an actuation electrode. The SRRs and the RF-MEMS can be combined following different configurations. In the configuration I (Fig. 5.19a), the external ring is used as DC ground electrode and is the anchor of the cantilever beams, while the internal ring,

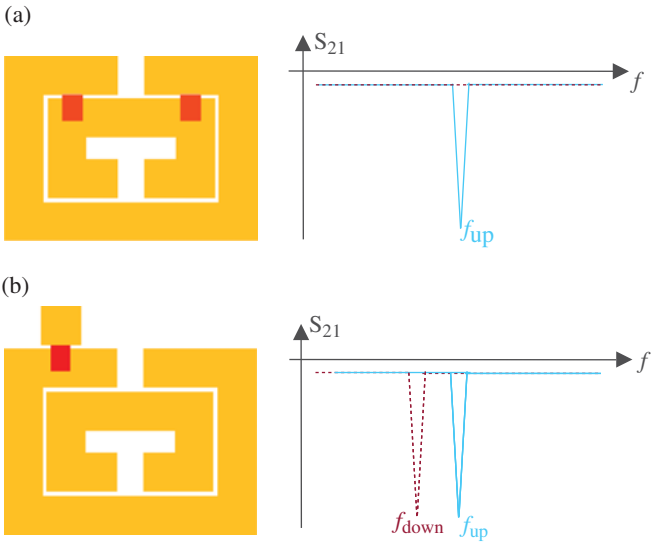

FIGURE 5.19 Illustration of cantilever-type RF-MEMS capacitive switches (represented by dark rectangles) loading a square SRR for configuration I (a) and II (b), as described in the text. The typical frequency responses of the tunable resonators coupled to a transmission line when all switches are at the up-state (solid lines) and when all switches are at the down-state (dotted lines), are also depicted. Reprinted with permission from Ref. [33]; copyright 2012 IOP Publishing.

under them and covered by a thin dielectric layer, acts as the DC actuation electrode. When the cantilever beams are at the up-state, the resulting capacitances formed with the internal ring are low. When they are actuated (down-state), the coupling between rings dramatically increases and this leads to a very large shift of the resonance frequency of the resonator. In the configuration II (Fig. 5.19b), the cantilever beam is anchored in a metallic patch and suspended over the outer ring. The switch actuation results in a resonance frequency decrement, and the frequency shift depends essentially on the metallic patch dimensions and location around the resonator.

The previous configurations can be applied to the implementation of compact tunable metamaterial-based filters at X-band, as will be shown in the illustrative examples. Extensive details on the fabrication of similar MEMS actuators are described elsewhere [35, 36]. Briefly, for the specific structures reported later, the actuation electrodes are realized by the thermal evaporation of a Cr/Au (60/1200 Å) thin layer on a 250 μm-thick Sapphire substrate (with dielectric constant $\varepsilon_r = 9.8$). They are covered by a 0.4 μm-thick Al_2O_3 dielectric layer deposited by plasma-enhanced chemical vapor deposition (PECVD). The alumina dielectric layer serves as electrical insulator between the lower electrode (outer ring of the SRR structure) and the MEMS cantilever beam (the upper moveable electrode, as shown in Fig. 5.2). It follows the lift-off of a 50 nm-thick doped Carbon layer, deposited by reactive laser ablation, to realize

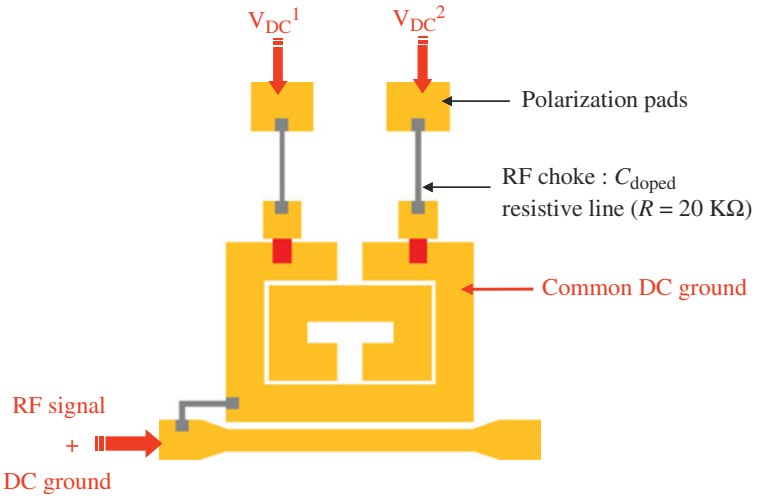

FIGURE 5.20 DC actuation principle in the case of a SRR in configuration II, with two cantilever beams independently actuated. Reprinted with permission from Ref. [33]; copyright 2012 IOP Publishing.

the 20 KΩ resistive lines (see Fig. 5.20 for the specific configuration II with the SRR coupled to a microstrip transmission line). The suspended parts of the structure (moveable cantilever beam) are defined by patterning a 0.5 μm-thick sacrificial polymethylglutarimide (PMGI) resist. The metallization is done using the Cr/Au seed layer which is gold-electroplated up to 1.5 μm. Next, a 90 Å Cr stress layer is deposited and patterned, in order to provide an appropriate stress gradient in the foldable areas. Finally, the device is realized and dried in a critical point drying system for avoiding stiction to the dielectric of the suspended structures. As illustrated in Figure 5.20, the structure integrates carbon-doped resistive lines and metallic polarization pads for the electrostatic actuation of the RF-MEMS switches.

On the basis of configuration I, stopband filters with electronically controllable number of poles can be implemented [33]. By this means, it is possible to tune the filter central frequency and the bandwidth. The idea is to couple multiple resonators, with slightly different resonance frequency, to the host line [37]. If the resonators are uncoupled, each resonator contributes with a filter pole (transmission zero) and bandwidth can be tailored. In the framework of this approach, it is clear that filter characteristics can be tuned by removing one or more resonators (and hence the corresponding poles). However, by using MEMS switches in combination with SRRs according to configuration I, the poles can be removed without the need for resonator removal. We simply need to actuate the MEMS, and the pole (or poles) of the corresponding SRR will be largely shifted. Following this idea, a four-pole reconfigurable bandstop filter, consisting of a 50 Ω microstrip transmission line loaded with four pairs of RF-MEMS-loaded SRRs, was designed and fabricated (Fig. 5.21) [33]. The difference between SRRs called A, B, C, and D is the side length H_i of the external ring (Fig. 5.21b), where $H_A = 1430$ μm, $H_B = 1475$ μm, $H_C = 1530$ μm, and

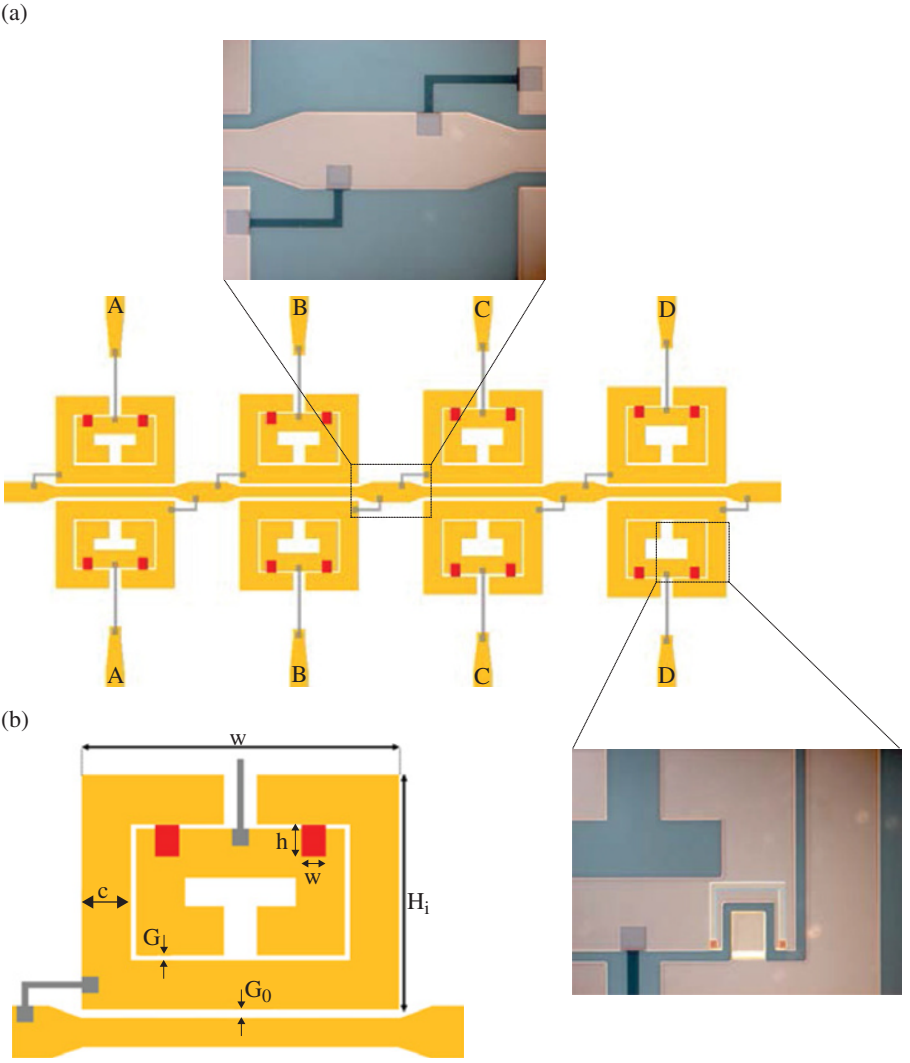

FIGURE 5.21 Layout of the four-pole reconfigurable band stop filter (a) and over scale view of one RF-MEMS-loaded SRR (b). The total size of the device is 6.4×14 mm^2. The dimensions of the cantilever-type MEMS are $h \times w = 200\ \mu\text{m} \times 150\ \mu\text{m}$. Width and distance between rings are $C = 300\ \mu\text{m}$ and $G = 30\ \mu\text{m}$. The gap between SRRs and the microstrip line is $G_0 = 50\ \mu\text{m}$. The side length of the SRRs in the longitudinal direction is $W = 1940\ \mu\text{m}$. Zoom photographs of the indicated parts of the fabricated device are also shown. Reprinted with permission from Ref. [33]; copyright 2012 IOP Publishing.

$H_D = 1580\ \mu\text{m}$. Without electrostatic actuation, this configuration provides a bandstop behavior with four poles corresponding to the resonance frequencies f_A (10.36 GHz), f_B (10.15 GHz), f_C (9.92 GHz), and f_D (9.73 GHz) of the SRRs of cells A, B, C, and D,

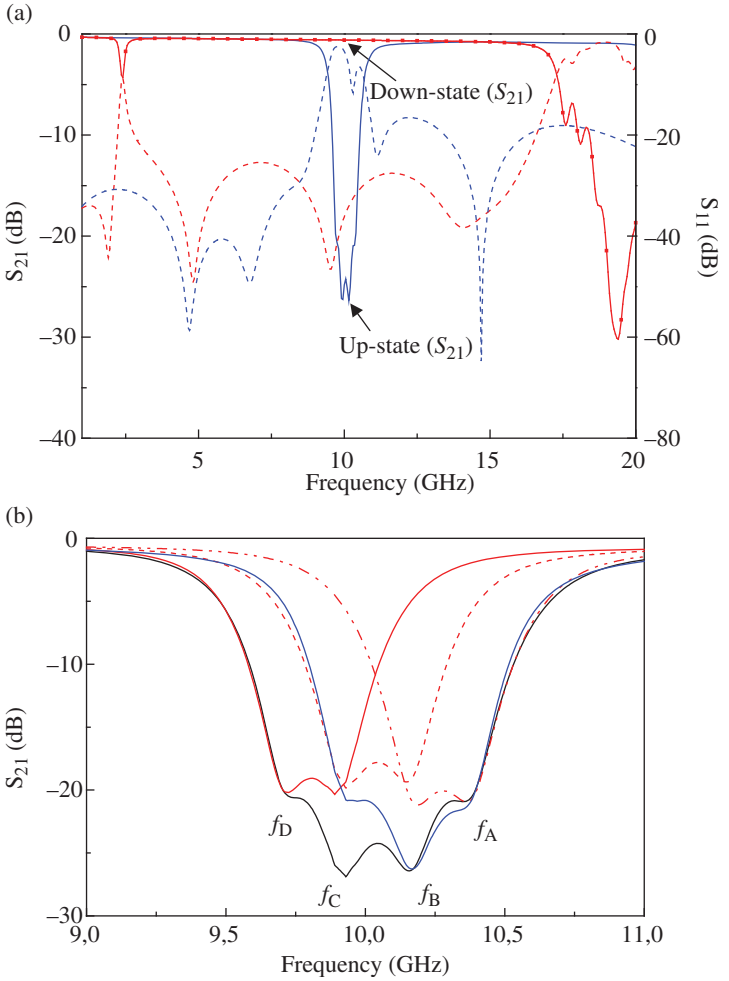

FIGURE 5.22 Simulated insertion (solid lines) and return (dashed lines) loss of the four-pole reconfigurable filter when all MEMS are at up-state and all MEMS are at down-state (a). Simulated responses of the device for different combinations of switches actuated (b). Reprinted with permission from Ref. [33]; copyright 2012 IOP Publishing.

respectively (Fig. 5.22). As shown in Figure 5.21a and b, the common DC ground signal is supplied to all external rings through the transmission line and resistive lines, while each internal ring acts as a DC-independent electrode. The reconfigurable filter, designed to operate at the X-band, was simulated by using the *Agilent Momentum* EM simulator. The ON/OFF RF-MEMS switches were designed to provide a ratio between up-state and down-state capacitances of 10, which leads to a shift of the resonance frequencies of the resonators from X-band to L-band. Owing to the actuation of switches and taking into account that both SRRs of one cell must always present

the same resonance frequency, we obtain a 4-bit (called A, B, C, and D) reconfigurable filter. The simulated S-parameters of the device are displayed in Figure 5.22a. When all switches are at up-state, the rejection is higher than 20 dB in a 0.7 GHz range. When they are all at down-state, insertion losses are less than 1 dB and return losses higher than 20 dB in a range from 3 GHz to 16 GHz. The curves in Figure 5.22b present other simulated filter responses corresponding to different bit-combinations. By varying the number of switches actuated, we can digitally tune the filter bandwidth and central frequency. The measured insertion and return losses of the filter with all MEMS at up-state (non-actuated) are presented in Fig. 5.23a and compared with the full wave simulations. As expected, the filter exhibits a four pole rejection band around 10 GHz and the rejection is higher than 20 dB on a 0.72 GHz frequency range. There is good agreement between simulation and experiment, except that out of the stopband measured insertion losses are higher and return losses are lower than those predicted by the simulation. This is due to the connection between the transmission line of the filter and the two SMA connectors. Other measured filter responses corresponding to different combinations of switches simultaneously actuated with 60 V are depicted in Figure 5.23b. The number of poles of the stopband corresponds to the number of non-actuated switches. With these results, the digital reconfigurability principle is validated.

The RF-MEMS-loaded SRRs of configuration II can be applied to the design of tunable bandpass filter. The topology of the considered filter, depicted in Figure 5.24, consists of a pair of coupled SRRs fed by 50 Ω microstrip transmission lines. In the proposed configuration, the electric coupling between these two adjacent resonant elements results in the bandpass behavior of the filter [38]. Such configuration provides also transmission zeros, present at both sides of the pass band, which are relevant for frequency selectivity improvement and are caused by the feeding structure, as discussed in Ref. [39]. Since the central frequency of the filter depends directly on the resonance frequency of the SRRs, the position of the filter pass band can be tailored by tuning the SRRs. On the other hand, bandwidth is mainly controlled by the coupling level between SRRs, which is scarcely dependent on MEMS actuation. Therefore, the proposed tunable filters are specifically designed to tune the filter central frequency. For the untuned state (nonactuated MEMS), there is a systematic approach for the design of these type of filters. That is, given filter specifications (bandwidth, order, central frequency, and minimum in-band return losses), the inter-resonator coupling coefficients and external quality factors are determined; and from these values, inter-resonator distance and the position of the feeding lines are determined [26]. However, since the main relevant aspect of this section is to highlight novel tuning concepts for artificial transmission lines based on RF-MEMS switches, rather than pursuing a specific frequency response for the considered type of tunable filter, the inter-resonator distance has been tailored in order to obtain a filter response with a fractional bandwidth (nonactuated switches) of roughly 15%.[7] In

[7] Indeed, the filter depicted in Figure 5.24, rather than being based on a tunable artificial transmission line, it is implemented following the well-known coupled resonator's approach. Nevertheless, it constitutes a good example to illustrate the potential of RF-MEMS-loaded SRRs in the design of tunable components, and for this reason it has been included in this section.

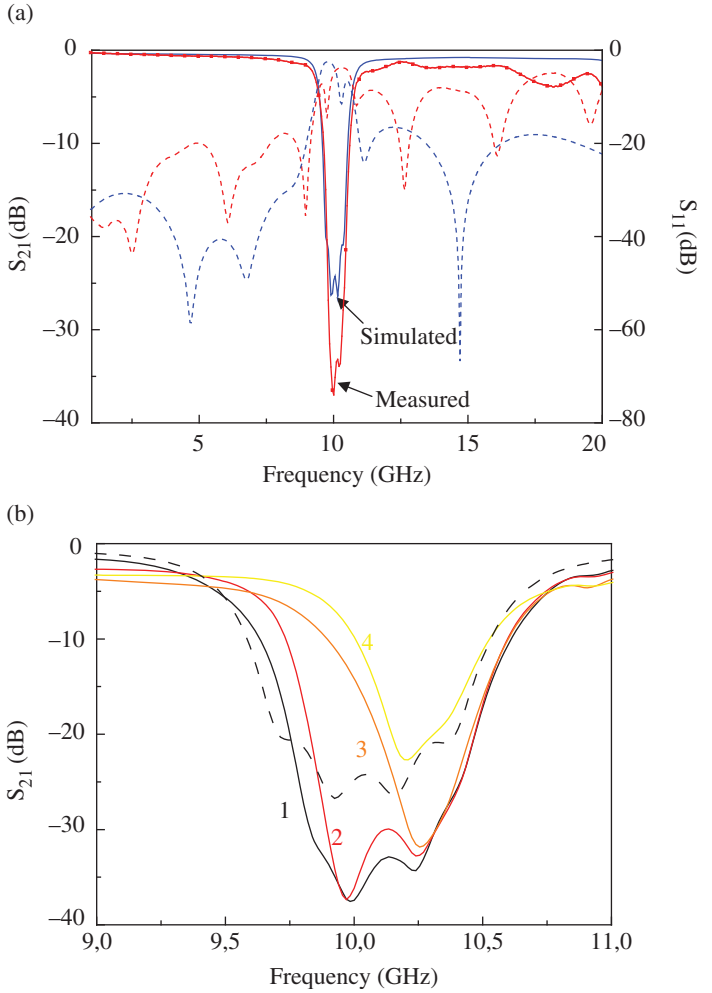

FIGURE 5.23 Simulated and measured insertion (solid lines) and return (dashed lines) loss of the four-pole reconfigurable stopband filter when all switches are at up-state (a). Simulated (dashed line) and measured (solid lines) responses of the device for different combinations of switches actuated (b). Measurements indicated as 1, 2, 3, and 4 correspond to bits ABCD set to "0000," "0001," "0011," and "1011," respectively, with "0" corresponding to MEMS at up-state (i.e., nonactuated) and "1" corresponding to MEMS at down-state. Notice that the bit combinations of (b) do not have direct correspondence to those of Figure 5.22b, except for the cases "0000," "0001," "0011." Reprinted with permission from Ref. [33]; copyright 2012 IOP Publishing.

order to improve the frequency selectivity of the filter, rather than considering a symmetric topology, a skew symmetric 0° feed configuration has been used, as reported in Ref. [39]. This produces one transmission zero at each side of the pass band, at those frequencies where the two signal paths between the feed point and the edges of the

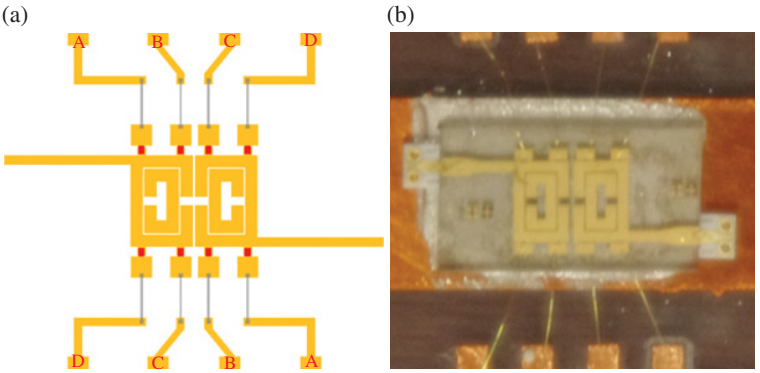

FIGURE 5.24 (a) Layout of the four-bit tunable bandpass filter. The geometrical parameters illustrated in Figure 5.21b are $h \times w = 200 \times 150$ μm, $C = 300$ μm, $G = 30$ μm, and $W \times H = 2190$ μm $\times$ 1490 μm. (b) Photograph of the fabricated device. Reprinted with permission from Ref. [33]; copyright 2012 IOP Publishing.

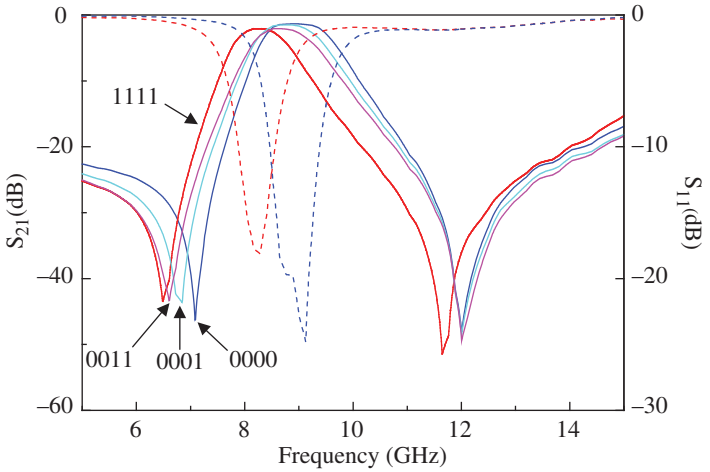

FIGURE 5.25 Measured insertion (solid line) and return (dashed line) loss of the designed digitally tunable bandpass filter for four different switching states. The switching states are "0000," "0001," "0011," and "1111," where the bit sequence is for the switches ABCD, and "0" and "1" stands for nonactuated and actuated, respectively. The return loss is only shown for the extreme states "0000" and "1111." Reprinted with permission from Ref. [33]; copyright 2012 IOP Publishing.

external ring are about one-quarter wavelength. The dimensions of the metallic patches to which the RF-MEMS are anchored determine the tuning range. The designed prototype was merely fabricated as a proof of concept; hence, the metallic patches were chosen with arbitrary dimensions. The measured frequency responses corresponding to four different states are depicted in Figure 5.25. The responses at

the two extremes correspond to all switches ON and OFF. From this, the tuning range is found to be roughly 10%. Filter performance is good, with measured in-band insertion losses (central frequency) of 1.3 dB and 2 dB at the two extremes of the tuning range, and return losses better than 35 dB in both cases. It is found that MEMS actuation does also shift down the transmission zero frequencies.

Tunable CSRRs using fixed-fixed beam RF-MEMS have been reported in Ref. [32]. The CSRRs are etched in the central strip of a CPW, and the RF-MEMS are implemented on top of them, as Figure 5.26 illustrates. Through electronic actuation, the MEMS are bended down, modifying the capacitance of the CSRRs and hence the resonance frequency. Thus, this configuration is useful for the implementation of tunable band stop filters. The prototype reported in Ref. [32], depicted in Figure 5.27, exhibits a tuning range of 20% and operates at the Q-band (for the interested reader, the details of the fabrication process are given in [32]). The

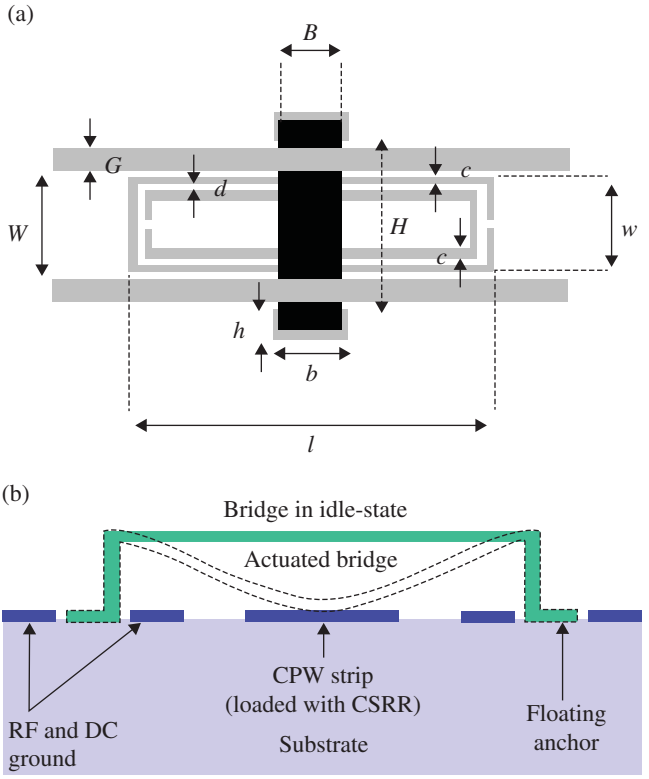

FIGURE 5.26 (a) Unit cell of the CSRR/RF-MEMS loaded CPW, with slot regions of the CPW depicted in gray, and relevant dimensions and (b) cross section of a CPW with a RF-MEMS bridge. The down-state corresponds to the application of an actuation voltage to the strip line of the CPW; in the up-state, no actuation voltage is applied. Reprinted with permission from Ref. [32]; copyright 2007 IET.

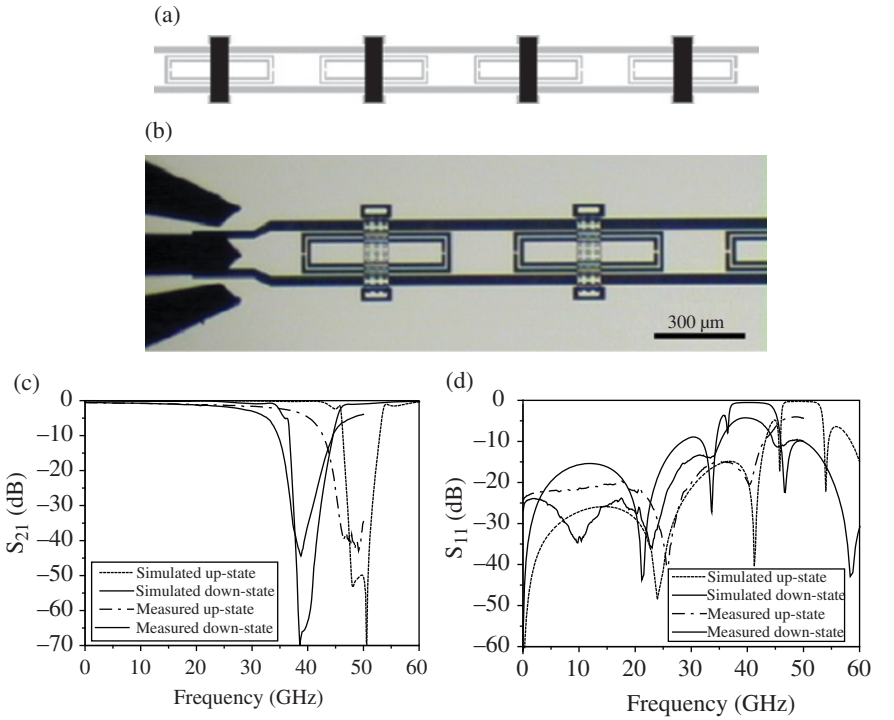

FIGURE 5.27 Layout of the fabricated tunable stopband filter (a), microphotograph of the first two stages of the filter, including RF probes (b), simulated and measured insertion losses (c), and simulated and measured return losses (d). The simulations were done by considering plate heights of 0.5 μm and 2 μm for the down- and up-state, respectively. Reprinted with permission from Ref. [32]; copyright 2007 IET.

dimensions of the CSRRs are (in reference to Fig. 5.26) $c = d = 10$ μm, $l = 480$ μm and $w = 130$ μm. CPW dimensions are: strip width $W = 150$ μm and slot width $G = 30$ μm. Finally, the geometry of the MEMS bridges is: $B = 80$ μm, $b = 100$ μm, $h = 40$ μm and $H = 290$ μm. The structure is a 4-stage periodic device where the distance between adjacent CSRRs is 220 μm. The simulated (by means of the *Agilent Momentum* by excluding losses) and measured S-parameters of the device are also depicted in Figure 5.27. As expected, the structure exhibits stopband behavior with tuning capability. The central frequency of the stopband is varied between 39 GHz and 48 GHz for corner actuation voltages of 17 V (down-state) and 0 V (up-state). This corresponds to a tuning range of roughly 20%. Measured rejection in the stopband is good ($IL > 40$ dB), whereas insertion losses in the allowed band are very small.

According to the results presented in this subsection, relative to SRRs and CSRRs loaded with RF-MEMS, it is clear that it is possible to implement tunable filters with very reasonable performance by using transmission lines loaded with these tunable metamaterial resonators. As compared to diode varactors, RF-MEMS not only

decrease the level of losses (especially critical in bandpass filters) but also allow for the implementation of tunable filters at very high frequencies.

Cantilever-Type SRRs An alternative approach for the implementation of tunable resonators consists of using the RF-MEMS as part of the SRR [34]. The rings forming the SRRs are partly fixed to the substrate (anchor) and partly suspended (up-curved cantilever). Through electrostatic actuation, the suspended parts are deflected down, the distributed capacitance between the pair of coupled rings is modified, and hence the resonance frequency of the SRR can be electrically tuned. A typical top view of the cantilever-type tunable SRR (rectangular shaped) is depicted in Figure 5.28a. The movable parts of the rings are indicated in gray. Obviously, we can arbitrarily select

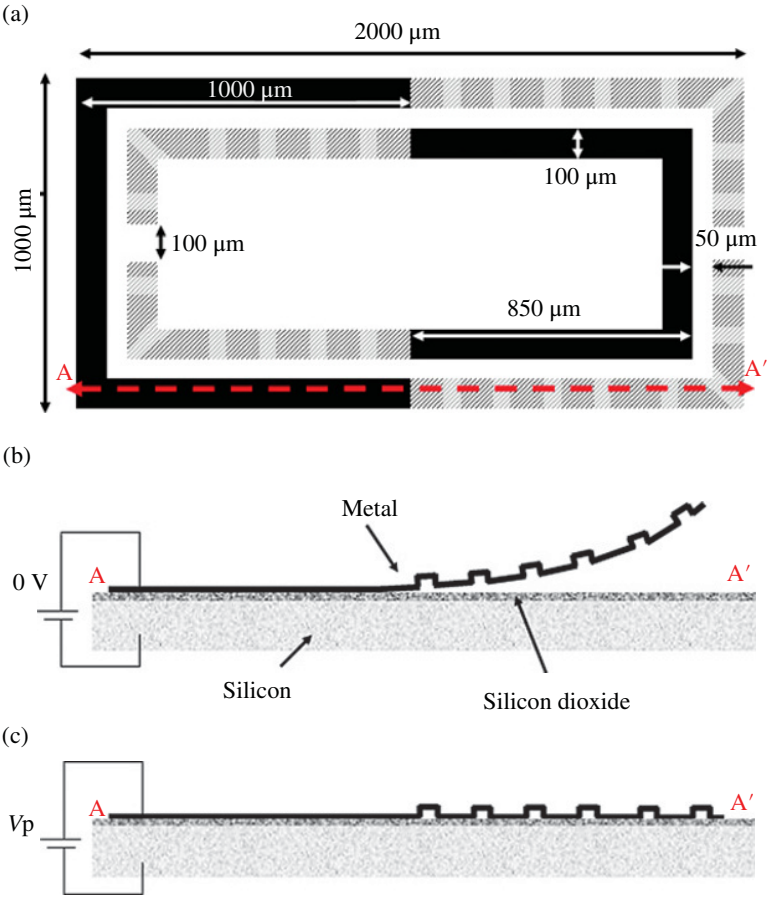

FIGURE 5.28 Tunable SRR based on cantilever-type RF-MEMS. (a) Top view with relevant dimensions. Black and gray parts correspond to anchors and suspended parts (including corrugations), respectively; (b) cross section in the up-state; (c) cross section in the down-state. Reprinted with permission from Ref. [34]; copyright 2011 IEEE.

the movable portion of each ring, which has direct influence on the tuning range. Figure 5.28b and c depict the cross-sectional view of the anchor and the cantilever, without (up-state) and with (down-state) electrostatic actuation, respectively. The tuning principle was validated in Ref. [34] by coupling the SRR of Figure 5.28 to a 50 Ω microstrip line (Fig. 5.29). Since we can independently actuate on both the internal and external ring of the tunable SRR, four different states arise. The measured transmission coefficients corresponding to the four states are also depicted in Figure 5.29. Without actuation (both cantilevers at up-state), the resonance frequency of the SRR is 13.42 GHz. It decreases to 11.45 GHz by actuating the outer ring or to 9.78 GHz by actuating the inner ring. The smaller resonance frequency (9.34 GHz) is that

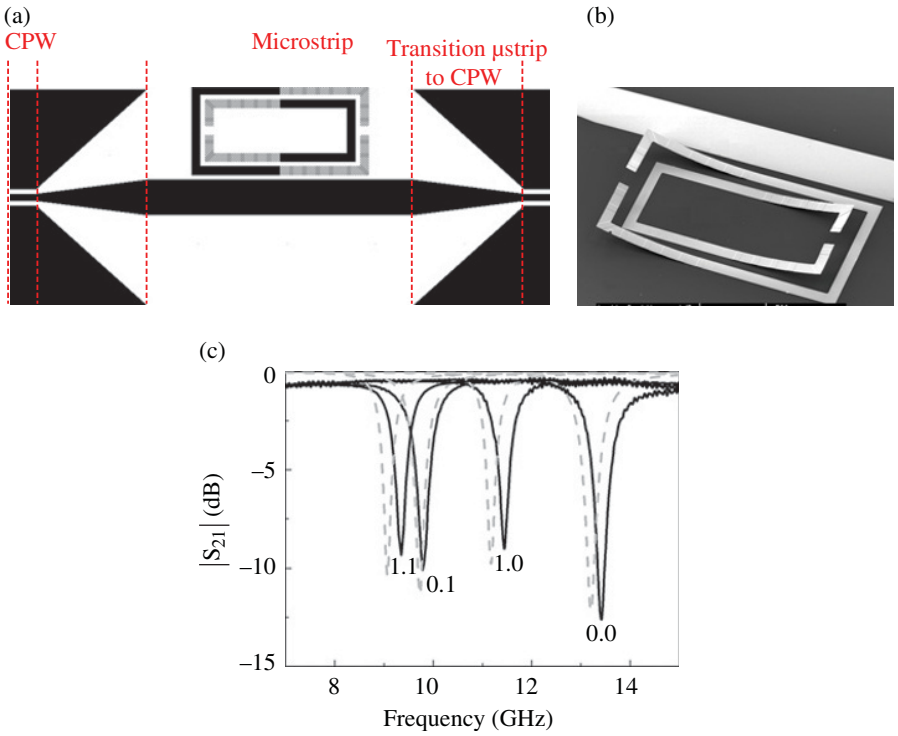

FIGURE 5.29 Topology of the tunable SRR coupled to a microstrip line with microstrip to coplanar waveguide transition (a), photograph of the nonactuated SRR (b), and measured (solid lines) and simulated (dashed lines) frequency response of the structure for the four different states (c). The separation between the SRR and the microstrip line is 50 μm, and the width of the microstrip line is 400 μm. The applied voltage for either ring actuation is 30 V. The state of the rings is indicated, where "1" (ring actuation) stands for down-state and "0" for up-state, and the first bit corresponds to the inner ring. Details on the fabrication process, substrate parameters and simulation are given in [34]. Reprinted with permission from Ref. [34]; copyright 2011 IEEE.

corresponding to the two rings in the down-state, as expected on account of the larger distributed capacitance between the two rings of the SRR.

By cascading the proposed MEMS-based SRRs in a microstrip transmission line, tunable stopband filters can be implemented (the rejection level can be controlled by the number of stages). Two prototype devices are depicted in Figure 5.30, where the

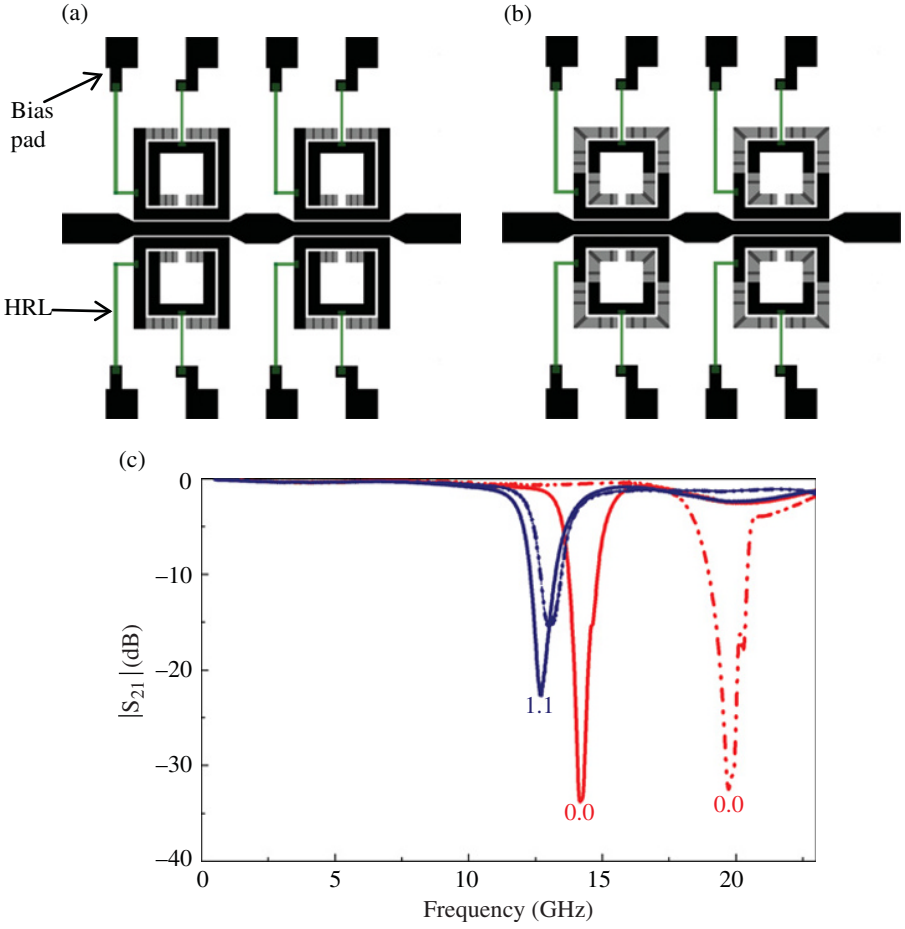

FIGURE 5.30 Tunable stopband filters based on square-shaped short (a) and long (b) cantilever-type SRRs, and measured transmission coefficients for the extreme switching states (c). SRR side length is 1200 μm, ring width 150 μm and ring separation 30 μm. The separation between the SRR and the microstrip line is 25 μm. The actuation voltages are applied to the rings through the bias pads and high resistive lines (HRLs). Solid lines correspond to the filter of (a) amd dash-dotted lines correspond to the filter of (b). As frequency decreases, rejection is reduced due to the degradation of the quality factor of the resonators (this aspect was discussed in Section 5.3.1.1). Actuation voltage is 30 V. Reprinted with permission from Ref. [34]; copyright 2011 IEEE.

difference between them is simply the length of the movable portions of the rings. The measured frequency responses corresponding to the extreme switching states ("00" and "11") are also depicted in Figure 5.30. The tuning range is 12% for the filter of Figure 5.30a and 42% for the one depicted in Figure 5.30b. This difference is due to the larger capacitance variations experienced with the prototype that uses longer cantilevers. As compared to tunable stopband filters based on SRRs and varactor diodes, the filters of Figure 5.30 exhibit better insertion losses in the allowed bands. As compared to the filters based on tunable RF-MEMS based CSRRs of Figure 5.27, the approach presented in this subsection, based on cantilever-type SRRs, can provide better tuning ranges.

5.3.1.3 Metamaterial Transmission Lines Based on Ferroelectric Materials

Ferroelectric materials have been used for tuning purposes in several microwave applications [40], particularly using ferroelectric varactors [15, 41] and planar resonators [42]. Tunable SRRs based on ferroelectric materials were first reported in Ref.[43], but the resonance frequency of those SRRs was modified by varying the temperature, rather than by the application of an external voltage. In [44], the dependence of the dielectric permittivity of ferroelectric materials with an external electric field was exploited in order to modify the resonance frequency of SRRs by means of an applied voltage (the resonance frequency of the resonators is modified by tailoring the distributed capacitance between the two rings forming the resonator, similar to the capacitance variation in interdigital varactors). These tunable resonators were then used as loading elements in a host line for the implementation of tunable stopband filters [44, 45].

The tunable SRRs in Refs [44, 45] were implemented by using a BST ($Ba_{0.6}Sr_{0.4}TiO_3$) thick-film with a thickness of 3.5 μm, made by screen-printing a Fe-F co-doped BST paste on an alumina substrate and sintering at 1200°C [46]. Based on this ceramic, the structured metallization for the strip of the transmission line and the SRR was realized by a single lithography step and plating 2.5 μm thick Au electrode on a Cr/Au seed layer which was afterwards removed by wet etching. A cross-section scheme of the substrate is depicted in Figure 5.31a. The biasing requires the connection of DC feeding lines and pads to the rings forming the SRR as shown in Figure 5.31b, where the relevant dimensions of the structure are also included. The *Rogers RO3003* substrate was used as carrier substrate for the whole device including the biasing network. The carrier substrate was placed on a copper plate that acts as microstrip ground and ensures mechanical stability. Due to the topology of the SRRs, no DC-blocking elements are needed, whereas the RF signal is blocked by means of 100KΩ SMD-resistors. Using the cell depicted in Figure 5.31b, an order-3 tunable stopband filter was designed [45] (Fig. 5.32a). The filter responses for the untuned (0 V) and tuned (140 V) states are depicted in Figure 5.32b. In the simulations, the employed values for the relative permittivity of the BST layer are $\varepsilon_{\mathrm{UNTUNED}} = 300$ and $\varepsilon_{\mathrm{TUNED}} = 220$, which fit the measurement curves and are typical values of the permittivity for the considered dimensions, tuning voltages and used BST material.

The application of BST thick films to the implementation of tunable composite right-/left-handed (CRLH) transmission lines based on the combination of OSRRs and OCSRRs was reported in Ref. [47]. These artificial tunable lines were then used

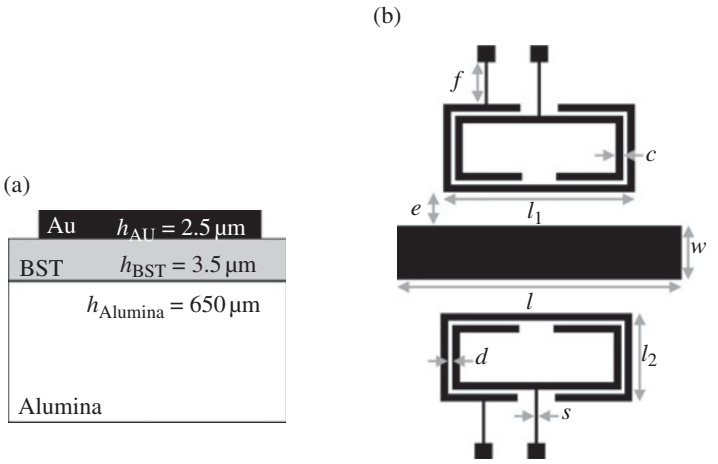

FIGURE 5.31 (a) Cross-section scheme of the substrate indicating layer thicknesses. (b) Layout of fabricated microstrip line and SRRs. Dimensions are $c = 100\,\mu m$, $d = 10\,\mu m$, $f = 590\,\mu m$, $s = 30\,\mu m$, $w = 520\,\mu m$, $l = 6.1$ mm, $l_1 = 3.1$ mm, $l_2 = 0.8$ mm, area $a = l_1 \times l_2 = 2.42\ mm^2 = 3.1\ mm \times 0.8\ mm = 0.07\lambda \times 0.02\lambda$ (λ is the guided wavelength at the resonance of the SRRs). Reprinted with permission from Ref. [44]; copyright 2009 IET.

for the implementation of tunable filters, phase shifters, and power dividers [48]. The structure reported in Ref. [47] (depicted in Fig. 5.33) consists of a CRLH unit cell implemented in CPW technology based on series connected OSRRs and a shunt OCSRR (with meandered lines to reduce dimensions). The fabrication process is similar to the one reported earlier, but the BST film has a thickness of 7.5 μm in this case. The relative permittivity of the BST in the untuned state is roughly $\varepsilon_r = 490$, and by applying a DC voltage, the permittivity can be reduced to approximately $\varepsilon_r = 220$, representing a material tunability of 55%. The equivalent circuit model of the structure is depicted in Figure 5.33c, where the variable capacitances are indicated. The series OSRRs are tuned by applying a voltage between the rings, through the feeding ports and the ground plane (the central strip and the ground plane of the CPW are electrically connected through the OCSRR). The tuning of the OCSRR requires two additional biasing lines inserted through the gaps of the rings since both rings are electrically connected. This biasing network is composed both of gold and chrome lines to avoid its RF influence on the biasing network, which could affect the band or the spurious response. The main advantage of this approach is that the biasing networks of the OCSRRs can be connected to the feeding ports, and hence the tuning of the whole artificial line can be achieved by applying only a single voltage between the feeding ports and the ground plane (which can be done directly from the probes). Further details are given in Refs [47, 48]. The measurement and EM simulations of the frequency response of the resulting topology are shown in Figure 5.33b. Notice that the CRLH line was not designed to satisfy given specifications. However the line is quasi-balanced, as revealed by the dispersion diagrams for the tuned and untuned states (Fig. 5.34). The reported structure exhibits good filtering behavior and tuning

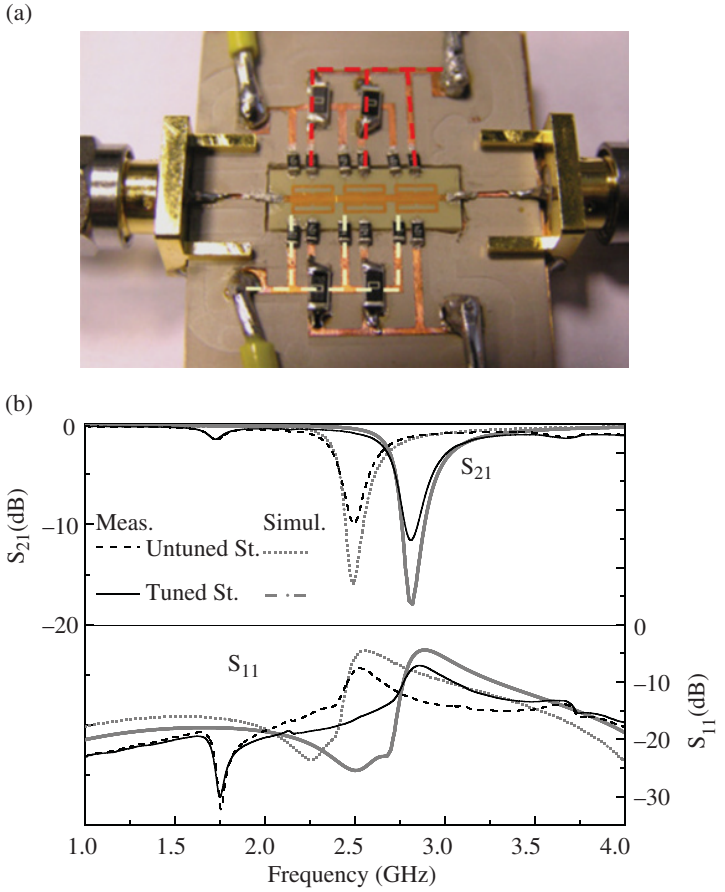

FIGURE 5.32 Photograph of the fabricated order-3 tunable BST-based filter (a), and measured and simulated frequency response of the device for the tuned (140 V) and the untuned (0 V) states (b). Two different parts of the biasing network are marked with dashed lines. For the tuned state, the one at the upper side corresponds to the 140 V, whereas the one at the lower side corresponds to 0 V. Reprinted with permission from Ref. [45]; copyright 2011 IET.

capability. However, to further control filtering characteristics, an independent control of the capacitance in the OSRRs and OCSRR is necessary. This aspect and the possibilities for the design of tunable filters and other microwave components based on CRLH lines are discussed in Ref. [48].

5.3.2 Tunable CL-Loaded Metamaterial Transmission Lines

Tunable CL-loaded metamaterial transmission lines can be designed by means of lumped varactors, ferroelectric varactors, RF-MEMS, and liquid crystals, among

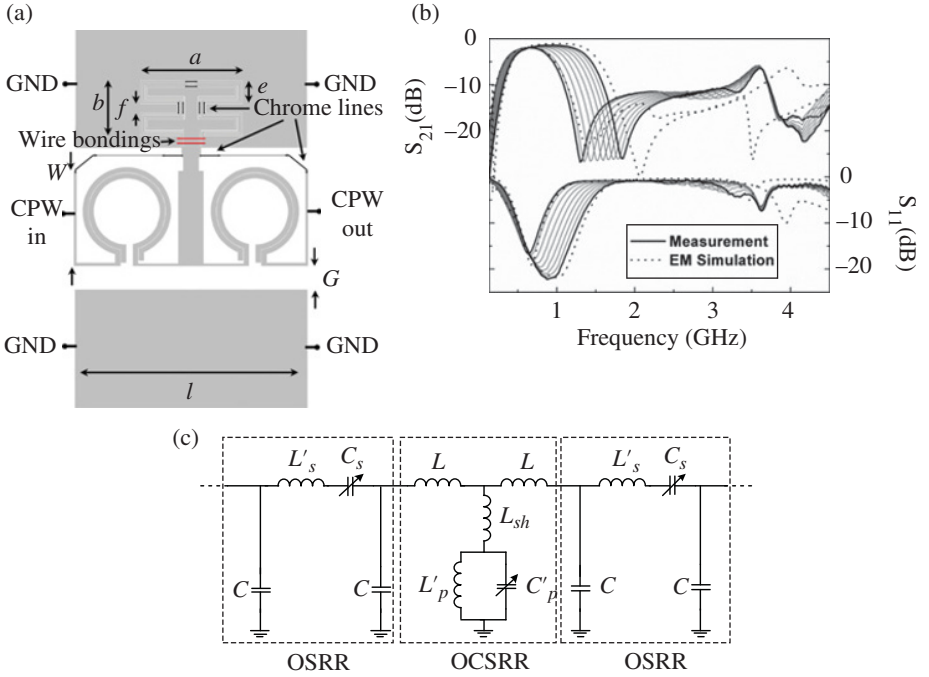

FIGURE 5.33 Layout (a) and measured response (b) of the tunable CRLH line, and equivalent circuit model (c). The tuning voltage is increased from 0 V up to 160 V in 8 steps. The indicated EM simulations, including losses, correspond to the maximum and minimum tuning states, considering the dielectric constants given in the text. The chrome lines are depicted in black. Wire bondings connecting the ground planes of the OCSRR are also needed to avoid slot modes. Dimensions are $l = 6.9$ mm, $W = 2.8$ mm, and $G = 0.72$ mm. For the OCSRR, $a = 3.05$ mm, $b = 1.66$ mm, $e = 0.7$ mm, $f = 0.26$ mm, $d = s = 60$ μm, and $c = 10$ μm, s being the width of the biasing networks between the rings of the OCSRR. For the OSRR, $r_{ext} = 1.3$ mm, $d = 10$ μm, and $c = 0.16$ mm. Reprinted with permission from Ref. [47]; copyright 2011 IEEE.

others. In the previous subsection, devoted to tunable resonant-type metamaterial transmission lines, the considered structures were grouped by technologies (this was mainly motivated by the different tuning strategies/approaches for the resonant elements corresponding to each technology, although the tuning principle was indeed the same). In this subsection, we have opted for presenting two illustrative applications of CL-loaded CRLH tunable lines, as representative examples: this includes a tunable phase shifter, implemented by means of diode varactors, and a liquid crystal-based tunable CRLH leaky wave antenna.

5.3.2.1 Tunable Phase Shifters CRLH-based tunable phase shifters using lumped varactors [49, 50], ferroelectric varactors [51], and RF-MEMS [52, 53] have been reported. As an example, the design of a tunable phase shifter, implemented by

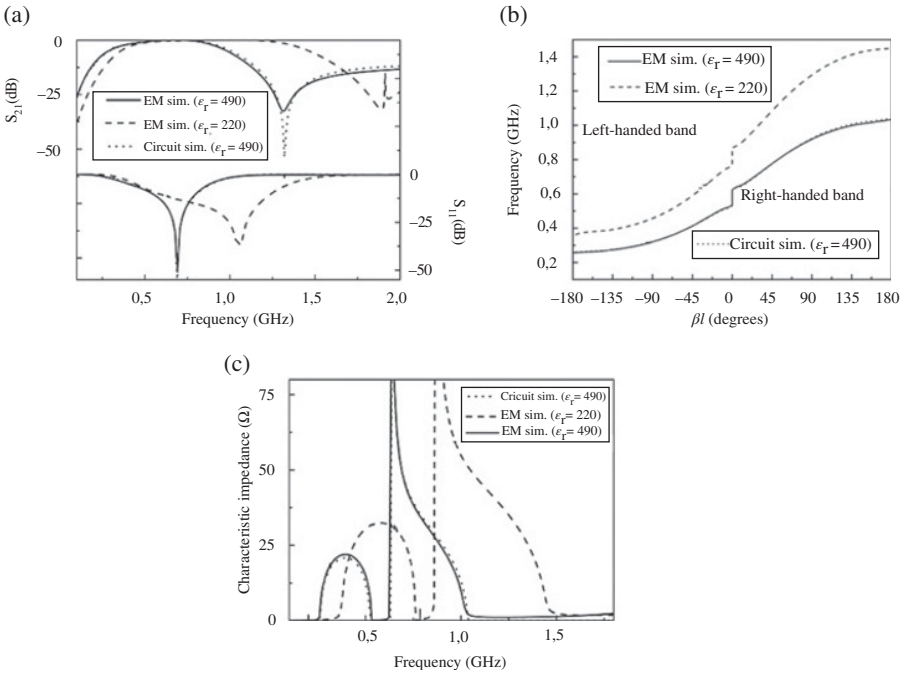

FIGURE 5.34 EM simulation of the S-parameters (a), dispersion diagram (b), and characteristic impedance (c) of the structure of Figure 5.33a for the maximum and minimum tuning states. The circuit simulation for the untuned state is also depicted. The equivalent circuit values are for the OSRR $C = 0.44$ pF, $L_s' = 5.25$ nH, $C_s = 16.87$ pF. For the OCSRR, $L = 0.27$ nH, $L_p' = 5.25$ nH, $C_p' = 10.27$ pF, and $L_{sh} = 1.93$ nH. Reprinted with permission from Ref. [47]; copyright 2011 IEEE.

means of varactor diodes, with separately tunable phase and line impedance [50], is reported. The independent tuning of phase and impedance reduces mismatch losses, allowing for a broadband behavior and a more constant insertion loss over all tuning states. The independent tuning principle is very simple. Assuming a lossless dual transmission line (Fig. 3.18a), in the homogeneous regime (long wavelength limit), the phase constant and the characteristic impedance are given by expressions (3.41) and (3.42). From these expressions, it follows that by tuning only one element (e.g., the capacitance), the phase shift can be tailored, but at the expense of a change in the characteristic impedance as well. However, since the line impedance is related to the quotient of the inductance and capacitance, it is possible to keep the line impedance constant by tuning both reactances by the same (dimensionless) factor, x, namely

$$\beta_L l(x) = -\frac{1}{\omega\sqrt{xL \cdot xC}} \tag{5.8}$$

$$Z_{\mathrm{BL}}(x)=\sqrt{\frac{xL}{xC}}=Z_{\mathrm{BL}} \tag{5.9}$$

Thus, an artificial line phase shifter that does not exhibit tuning induced mismatch is possible. However, a purely left-handed (PLH) line cannot be implemented in practice. Including the parasitics of the host line, a CRLH transmission line results, and the corresponding phase and characteristic impedance are given by expressions (3.51) and (3.52). In the long wavelength limit, these expressions can be written as follows:

$$\beta=\frac{s(\omega)}{l}\sqrt{\omega^2 L_{\mathrm{R}}C_{\mathrm{R}}\left(1-\frac{1}{\omega^2 L_{\mathrm{R}}\cdot xC_{\mathrm{L}}}\right)\left(1-\frac{1}{\omega^2 C_{\mathrm{R}}\cdot xL_{\mathrm{L}}}\right)} \tag{5.10}$$

$$Z_{\mathrm{B}}=\sqrt{\frac{L_{\mathrm{R}}}{C_{\mathrm{R}}}\frac{\left(1-\dfrac{1}{\omega^2 L_{\mathrm{R}}\cdot xC_{\mathrm{L}}}\right)}{\left(1-\dfrac{1}{\omega^2 C_{\mathrm{R}}\cdot xL_{\mathrm{L}}}\right)}} \tag{5.11}$$

where tuning, associated to the series capacitor and shunt inductor, has been included. Notice that (5.10), is identical to (3.59), but it has been expressed as shown, in order to appreciate the tuning elements. Inspection of (5.11) reveals that, in general, the terms in the parenthesis do not cancel. However, by balancing the line, that is, $L_{\mathrm{R}}C_{\mathrm{L}}=L_{\mathrm{L}}C_{\mathrm{R}}$, the characteristic impedance becomes constant over the tuning interval.

To avoid the use of tunable inductances, the strategy used in Ref. [50] consists of replacing such elements with tunable varactors in conjunction with transmission line impedance inverters. The circuit schematic of the tunable line is depicted in Figure 5.35, where the effective tuning voltages for the shunt and series varactors are U_1 and U_2, respectively. The inductors at the feeding points are RF chokes and are used to decouple the RF signals from DC polarization. The capacitors cascaded to the shunt varactors are virtual grounds for the RF signals. In Ref. [50], the 10nH inductor *LQW15AN10H00* from *Murata* for RF decoupling, and the 10 pF capacitor *500S100* from *American Technical Ceramics* for virtually grounding were used. The employed varactor diode was the *Infineon BB857* since it has a very low series inductance of 0.6 nH. Optimization of the transmission lines was done since it was found that the characteristic impedance of such lines controls the value of the realized inductance whereas the length controls the amount of variation of such inductances with frequency [50]. The details of prototype fabrication and calibration are out of the scope of this book and can be found in Ref. [50]. The photograph of the fabricated device is shown in Figure 5.36a. Figure 5.36b plots the transmission phase, considering $U_1=U_2$, with tuning voltage steps of 4 V. The phase curves are equidistant for equidistant tuning voltages, so the phase is a linear function of the tuning voltage. The quality of the phase shifter is generally estimated from the following figure of merit (FoM), which relates the obtainable phase shift to the incurred transmission losses [50]:

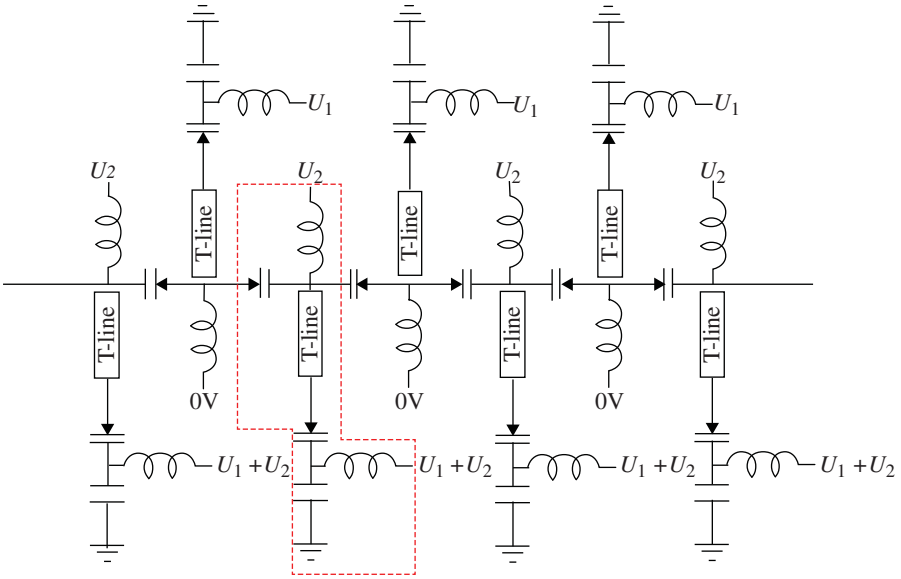

FIGURE 5.35 Schematic of the tunable phase shifter with independent tuning. Reprinted with permission from Ref. [50]; copyright 2006 EuMA.

$$\text{FoM} = \left| \frac{\varphi(C_2) - \varphi(C_1)}{\min\left(|S_{21}(x)|_{\text{dB}}\right)} \right| \quad x \in [C_1, C_2] \tag{5.12}$$

where C_1 and C_2 denote two tuning states and $\varphi(C_{1,2}) = \angle S_{21}(C_{1,2})$. Thus, the FoM is optimized if the phase shift variation experienced in the tuning range is large and the maximum attenuation ($\min(|S_{21}(x)|_{\text{dB}})$) occurring in the same tuning range is small. The measured FoM for tuning states with $U_1 = U_2$ is depicted in Figure 5.36c, where it can be appreciated that the FoM is larger than 60°/dB in a 30% bandwidth (around 6.5 GHz). In the same figure, the variation of the transmission magnitude over all tuning states from maximum to minimum differential phase shift is also included. In an ideal phase shifter the amplitude variation of the signal is zero, but the measured result (below 2.5 dB in the above cited bandwidth) is very reasonable.

5.3.2.2 Tunable Leaky Wave Antennas (LWA) Tunable LWAs have been implemented by means of CRLH lines using varactor diodes [54, 55], RF-MEMS [56], and liquid crystals [57, 58]. As an illustrative example, let us now focus on the LWA reported in Ref. [58], operative in the Ka-band, and able to provide beam steering for fixed operation frequency. Beam steering as a function of frequency (frequency tuning) in CRLH-based LWAs is consequence of the dispersive characteristic of the phase constant in CRLH lines (as it was discussed in Chapter 4). However, for many applications beam steering is desirable at a fixed frequency. Using varactor diodes, fixed frequency beam steering was achieved in Ref. [54]. However, semiconductor

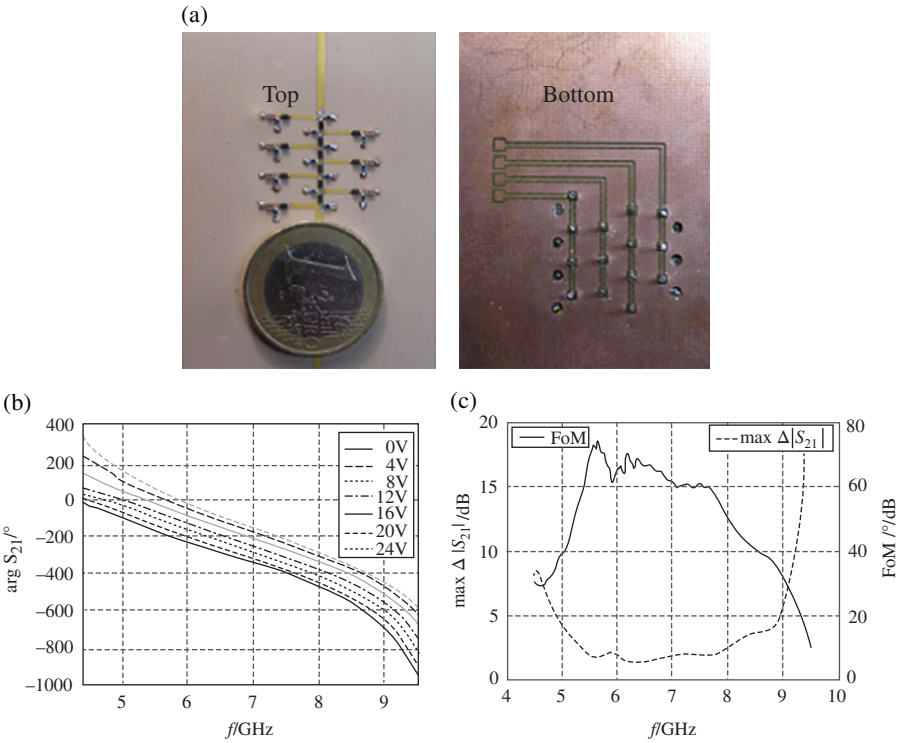

FIGURE 5.36 Photograph of the fabricated phase shifter (a), transmission phase (b), and FoM (c). The top layer is the RF part of the device with SMD components and signal lines, whereas the bottom layer is the DC feeding network. The ground plane for RF is sandwiched between these layers, so that the structure has three metal layers. The upper dielectric is the *Rogers RO3011* (0.51 mm thickness) and the bottom one is FR4 (1.4 mm thickness). Reprinted with permission from Ref. [50]; copyright 2006 EuMA.

varactors are frequency limited (i.e., they exhibit poor performance at high frequencies), and advanced technologies/materials, such as liquid crystals (acting as a continuously tunable anisotropic dielectric), are preferred for operation at high frequencies. The tuning of the phase constant, and hence the radiation angle, is achieved by tuning the liquid crystal (this can be done through magnetic or electric field actuation, as indicated in Section 5.2.4).

The unit cell layout of the antenna is depicted in Figure 5.37, and it consists of series-connected interdigital capacitors (C_L) alternating with meandered shunt inductors (L_L). At the extreme of the shunt inductors, interdigital (blocking) capacitors introduce an additional capacitance (C_{DC}) necessary for tuning by application of a bias voltage (in spite that tuning in Ref. [58] is carried out by means of magnetic field actuation). The parameters of the host line (L_R and C_R) complete the circuit model of the unit cell, also depicted in Figure 5.37. The capacitance C_{DC} introduces a transmission zero below the first LH band, but this transmission zero is not relevant for the

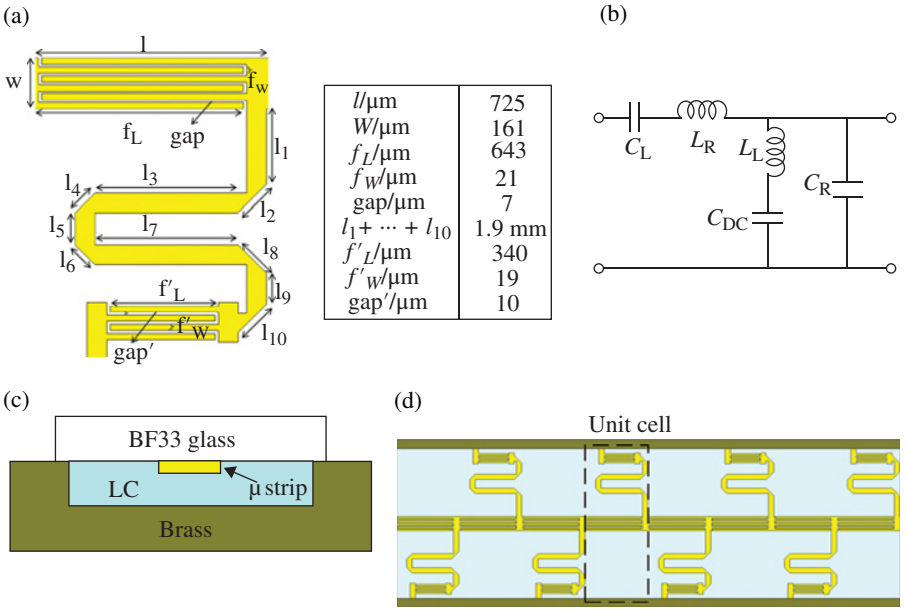

l/μm	725
W/μm	161
f_L/μm	643
f_W/μm	21
gap/μm	7
$l_1 + \cdots + l_{10}$	1.9 mm
f'_L/μm	340
f'_W/μm	19
gap′/μm	10

FIGURE 5.37 Unit cell layout, including dimensions (a), unit cell circuit model (b), cross section (c), and top view (d) of the liquid crystal-based tunable LWA. Reprinted with permission from Ref. [58]; copyright 2013 EuMA.

functionality of the structure as a tunable LWA.[8] Figure 5.37c and d show the cross sectional and top view of the LWA (actually the antenna is composed of 15 cells, although only eight cells are shown in the figure). As detailed in Ref. [58], the antenna was printed on the bottom side of a borofloat (BF33) glass substrate with dielectric constant $\varepsilon_r = 4.65$ and $\tan\delta = 0.008$. The metallic strips, made of gold, have a thickness of 2 μm. A polyimide layer was spin coated with a height of typically 10–100 nm and subsequently mechanically rubbed with a velvet cloth to anchor the liquid crystal molecules in the unbiased state parallel to the rubbing direction [59]. A metal block was used as ground plane and to provide mechanical stability. The glass substrate was glued with conducting glue on top of the metal block forming a 100 μm cavity. The cavity was filled with the liquid crystal *TUD-649* with $\varepsilon_{r\perp} = 2.43$, $\varepsilon_{r\parallel} = 3.22$, $\tan\delta <$ 0.0066 and sealed with two-component epoxy glue. The orientation of the liquid crystal molecules and, therefore, its permittivity can be tuned either by applying static electric or magnetic field, although the latter was chosen in the proof-of-concept prototype presented in Ref. [58]. For that purpose, rare earth magnets with field strength of 0.3 T were used.

The description of the experimental setup and further details on the interface between the LWA and the connectors (necessary for far-field measurements) are

[8] Notice that with interdigital capacitors, it is very difficult to achieve the necessary high capacitance values to virtually ground the meandered inductors for RF signals.

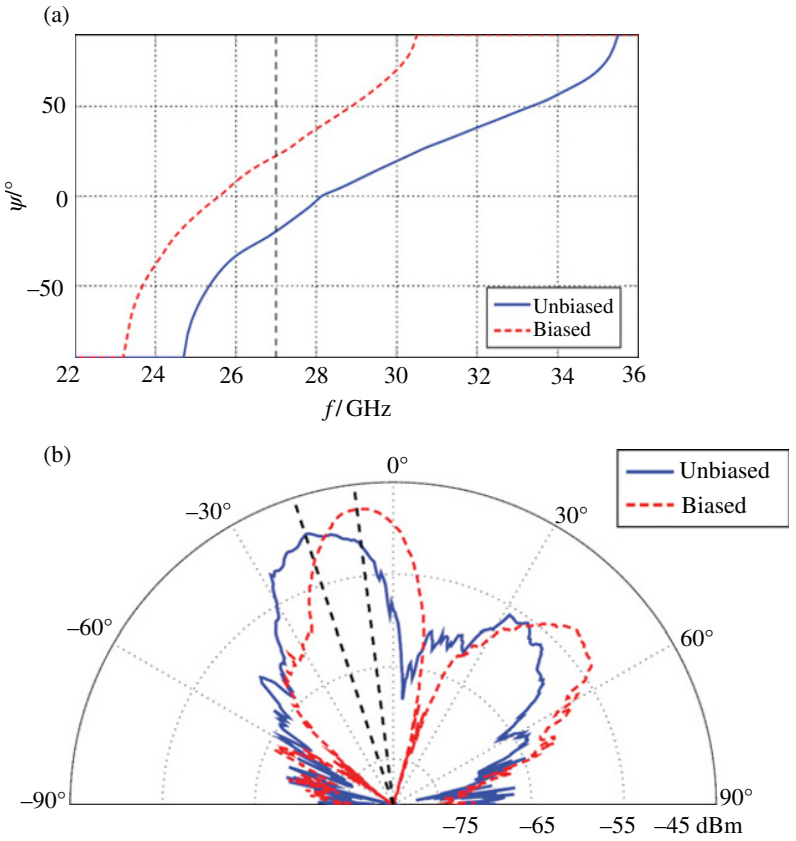

FIGURE 5.38 Radiation angle of the LWA inferred from the measured dispersion diagrams for the biased and unbiased states (a), and measured far-field radiation patterns at 27 GHz (b). Reprinted with permission from Ref. [58]; copyright 2013 EuMA.

given in Ref. [58]. From the measured dispersion for the biased and unbiased states, the radiation angle as a function of frequency was obtained (using expression 2.11). The results are depicted in Figure 5.38a, and indicate that for a fixed frequency of 27 GHz, it is possible to achieve a beam steering range from roughly −20° to +20°, going through the broadside direction if the liquid crystal orientation is continuously tuned. The measured far-field pattern at 27 GHz (depicted in Fig. 5.38b) reveals that for the unbiased state the radiation angle of the main beam is very close to the predicted value. However, for the biased state the main beam points to −7°. The good agreement of the unbiased state and the decreased scanning range indicate that the liquid crystal molecules are not completely oriented in the biased state in the far-field measurements. This was attributed in Ref. [58] to the larger distance of the rare earth magnets that had to be placed behind the antenna, in comparison to the on-wafer measurements (for measuring the dispersion diagrams), where the biasing magnets were placed directly under the glass substrate and thus, closer to the liquid crystal. Nevertheless, the tuning

principle and the potentiality of liquid crystals for the implementation of high-frequency tunable LWAs based on CRLH lines are demonstrated.

To end this section, devoted to tunable and reconfigurable devices based on artificial transmission lines, we would like to mention that only a representative subset of the reported approaches, technologies, and applications has been presented. Many other tunable components (i.e., couplers, filters, impedance matching networks etc.) based on artificial transmission lines can be found in the literature (some additional references for those interested readers are Refs [60–66]).

5.4 NONLINEAR TRANSMISSION LINES (NLTLs)

NLTLs are periodic structures implemented by loading a transmission line with nonlinear elements, typically shunt-connected voltage-dependent capacitances. In the linear regime, these structures exhibit a slow-wave behavior (see Chapter 2), and the phase and group velocity can be tuned by virtue of the controllable effective capacitance of the line. In the nonlinear regime, NLTLs are very interesting structures that can be used to achieve pulse and impulse compression or harmonic generation (frequency multipliers) [67]. In NLTLs, there are two main effects that give rise to the rich phenomenology that these artificial lines exhibit: nonlinearity and dispersion. Dispersion is related to periodicity, whereas the voltage variable capacitances are responsible for nonlinearity. In the limit of weak dispersion,[9] wave propagation is dominated by the nonlinearity, with the effect of steepen the falling edge of a voltage waveform. This effect can be intuitively explained by considering the voltage-dependent capacitance of a varactor diode or a HBV (it decreases with the absolute value of the applied voltage). The instantaneous propagation velocity at any given point in space and time is inversely proportional to the square root of the effective capacitance. Since such capacitance is smaller for higher voltages, the result is that the points closer to the crest of the voltage waveform experience a faster propagation velocity and produce a shock-wave front. With this approach, fall times in the vicinity of 1 ps are possible [67].

However, the most intriguing aspect of NLTLs appears when both dispersion and nonlinearity are simultaneously present. Dispersion tends to spread out voltage pulses propagating in the line, whereas nonlinearity has the opposite effect. Under certain conditions both effects balance, giving rise to the propagation of electrical pulses with permanent profile, that is, solitons[10] [68]. Thus, solitons are electrical pulses that propagate in the line without distortion, and are the consequence of the combined effects of nonlinearity and dispersion. The concept of solitary wave was introduced by John Scott Russell in 1844 [69]. Solitons have been an object of research interest in several fields, including mathematics, applied physics (mainly optics [70, 71]), and electronics [67, 72, 73]. In the latter case, soliton propagation in NLTLs has been studied due to the ability of these lines to generate harmonics from the decomposition of the input

[9] Weak dispersion conditions are met if the frequency components of the waveform are small compared to the Bragg frequency. See Chapter 2 for more details.

[10] It is assumed that the NLTL is lossless. Otherwise, pulse amplitude progressively decreases.

signal into their constitutive solitons [67]. One fundamental property of NLTLs supporting soliton wave propagation is the fact that any input signal not being a soliton tends to progressively decompose in a set of solitons with different amplitudes and velocities. Therefore, frequency multiplication in NLTLs can be interpreted as due to the generation of various solitons per semicycle of the input waveform. Besides the above fundamental property, larger amplitude solitons are narrower and travel faster than lower amplitude solitons. Moreover, solitons of different amplitude (and hence pulse velocity) that collide preserve their identity after the collision.

In monolithic NLTLs, solitary pulses of picosecond duration can be supported. Hence, these lines are interesting for the generation of signals with high frequency harmonic content (i.e., up to hundreds of GHz and even THz) on the basis of frequency multipliers based on them. In the nineties, monolithic NLTLs were considered as firm candidates for the implementation of signal sources in the so-called THz gap [74–80] on the basis of harmonic generation from smaller frequency signals. One advantage of NLTLs as frequency multipliers is their potential for the suppression of high-order harmonics. This is due to the intrinsic low-pass filtering behavior of these lines, related to periodicity, which precludes wave propagation in a wide band above the Bragg frequency (see Chapter 2). For frequency triplers, for instance, it is possible to suppress the fourth- and higher-order harmonics by properly designing the lines (i.e., with the Bragg frequency set slightly above the third harmonic of the reference frequency).[11] On the other hand, the second and even-order harmonics can be suppressed by using nonlinear devices exhibiting a symmetric (even) capacitance-voltage characteristic, as occurs with HBVs (this was anticipated in Section 5.2.1). With such even nonlinear capacitance–voltage function, if the HBV is excited by a harmonic voltage, it produces a current with frequency components at the fundamental frequency and odd harmonics only. The reason is that the current can be expressed as an odd function of the applied voltage, and cancelation of the even harmonics results. A similar argument can be applied to explain even-order harmonic cancelation in NLTLs loaded with devices exhibiting a symmetric capacitance–voltage characteristic. This cancellation of undesired harmonics is important for conversion efficiency optimization (excellent HBV tripler results, demonstrating an efficiency of 12% at 247 GHz, were reported in Ref. [81]).

To gain more insight on soliton wave propagation in NLTLs, a simple model is presented in the next subsection, and then some illustrative results showing the decomposition of a feeding signal into solitary pulses are provided.

5.4.1 Model for Soliton Wave Propagation in NLTLs

Figure 5.39 shows the schematic of a NLTL together with the lumped-element equivalent circuit model, which has been used to study harmonic multiplication [79, 82] and pulse sharpening [83]. L and C_o are the per-section inductance and capacitance, respectively, of the line, while $C_D(V)$ represents the nonlinear device capacitance. The study of soliton propagation in nonlinear networks of the type of Figure 5.39b was already carried out by Hirota and Suzuki [84] in the seventies. They considered

[11] In the context of this section, the harmonic order n is related the fundamental frequency, f_o, by $f_n = nf_o$.

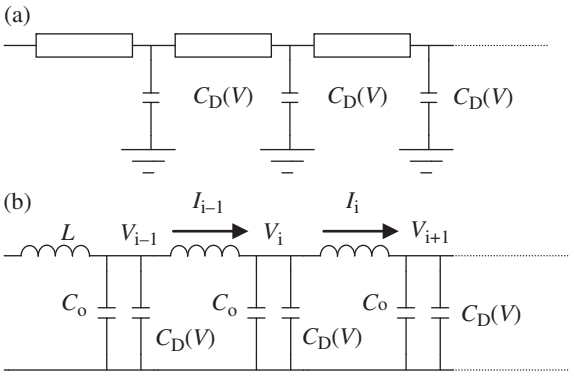

FIGURE 5.39 NLTL circuit schematic (a) and lumped-element equivalent circuit (b). Each transmission line section between nonlinear capacitances is modeled by a series inductor, L, and shunt capacitor, C_o.

a nonlinear shunt capacitance of the form $C(V) \propto 1/(V-V_o)$ (where V_o is a constant). In this particular case, the system is equivalent to the Toda lattice [85], for which soliton solutions are well known, and can be described by the Korteweg–de Vries (KdV) equation [86] in the long wave limit (i.e., nonlocalized solitons). Systems based on the KdV equation have been well studied, and the response of such systems to initial disturbances that break up into solitons has been described by the inverse scattering method [72]. However, for strong lumped solitons, or to study soliton propagation in nonlinear *LC* networks with arbitrary capacitance–voltage nonlinearity, a KdV approach can not generally be applied.

In this subsection, a simple procedure to obtain approximate soliton solutions in NLTLs described by its lumped-element equivalent circuit (Fig. 5.39b) is presented [87, 88], and applied to structures with HBV-like nonlinear devices (a similar model that considers MOS varactors to sharpen the rising and falling edge of a pulse was reported in Ref. [89]). The lumped model is accurate enough in the long wavelength limit, and it provides a reasonable description of NLTLs up to frequencies close to the cut-off (Bragg) frequency if $C_D(V) \gg C_o$, as it was discussed in Chapter 2 (and demonstrated in [87, 88]). A more sophisticated model [90] using the microwave circuit theory to explicitly simulate each transmission line section, has been developed to study high-frequency components of picosecond pulse generation with NLTLs. Nevertheless, the main interest of this Section is to analyze the effects of line parameters and nonlinearity on soliton characteristics (amplitude, width, and velocity). To this end, the proposed model suffices, and it is useful as guideline for the design of frequency multipliers based on NLTLs.

In view of Figure 5.39b, the voltage drop at the inductors with currents designated as I_{i-1} and I_i is

$$V_{i-1}(t) - V_i(t) = L \cdot \frac{dI_{i-1}(t)}{dt} \tag{5.13a}$$

$$V_i(t) - V_{i+1}(t) = L \cdot \frac{dI_i(t)}{dt} \tag{5.13b}$$

respectively. By subtracting the previous equations, it follows:

$$V_{i-1}(t) - 2 \cdot V_i(t) + V_{i+1}(t) = L \cdot \frac{d(I_{i-1}(t) - I_i(t))}{dt} \tag{5.14}$$

Taking into account that the I_{i-1}–I_i is the displacement current at the capacitance $C(V) = C_o + C_D(V)$, i.e.,

$$I_{i-1}(t) - I_i(t) = C(V_i(t)) \frac{dV_i(t)}{dt} \tag{5.15}$$

expression (5.14) can be written as:

$$L\left(C(V_i(t)) \frac{d^2 V_i(t)}{dt^2} + \left(\frac{dV_i(t)}{dt} \right)^2 \frac{dC(V)}{dV} \right) = V_{i-1}(t) - 2 \cdot V_i(t) + V_{i+1}(t) \tag{5.16}$$

In order to simplify this equation, we employ a standard continuum limit [72] for the voltage, that is, $V_i(t) \rightarrow V(x, t)$, where $x = i \cdot l$ and l is the distance between nonlinear capacitors. Within this limit, a Taylor expansion up to the fourth order can be carried out:

$$\begin{aligned} V_{i \pm 1}(t) = V(x \pm l, t) \approx V(x,t) \pm \frac{\partial V(x,t)}{\partial x} \cdot l + \frac{1}{2} \frac{\partial^2 V(x,t)}{\partial x^2} \cdot l^2 \pm \frac{1}{3!} \frac{\partial^3 V(x,t)}{\partial x^3} \cdot l^3 \\ + \frac{1}{4!} \frac{\partial^4 V(x,t)}{\partial x^4} \cdot l^4 \end{aligned} \tag{5.17}$$

Moreover, solitons moving at a propagation velocity v have a static profile in a new time coordinate system given by $s = t - x/v$. With this new variable, $\partial/\partial x = -1/v \cdot d/ds$ and $\partial/\partial t = d/dt$. In this way, Equation 5.16 can be rewritten as follows:

$$L \frac{d}{ds} \left(C(V) \frac{dV(s)}{ds} \right) = T^2 \frac{d^2 V(s)}{ds^2} + \frac{T^4}{12} \cdot \frac{d^4 V(s)}{ds^4} \tag{5.18}$$

where T is the per-section propagation delay, that is, $T = l/v$. Integration of (5.18) gives:

$$\left(C(V) - \frac{T^2}{L} \right) \frac{dV(s)}{ds} = \frac{T^4}{12L} \frac{d^3 V(s)}{ds^3} \tag{5.19}$$

where the independent term is null, provided odd order derivatives vanish at pulse maximum ($s = 0$), and we are seeking for localized solutions whose derivative tends to zero when $s \to \pm\infty$. Equation 5.19 can be integrated again to give:

$$F(V(s)) - \frac{T^2}{L}V(s) = \frac{T^4}{12L}\cdot\frac{d^2V(s)}{ds^2} \tag{5.20}$$

where $F(V)$ is a function responsible for non linearity defined as follows:

$$F(V) = \int_0^V C(V')dV' \tag{5.21}$$

In Figure 5.40, $F(V)$ obtained from the nonlinear capacitance given in the caption is depicted. The slope of this function asymptotically approaches C_o, the per-section capacitance of the line, while at zero bias the derivative is given by $C_o + C_D(0)$. An analysis of Equation 5.20 for $s \to \pm\infty$ indicates that the integration constant is zero since all terms vanish at this limit.

Inspection of Equation 5.20 reveals that solitary wave solutions are possible. To demonstrate this, the second term of the left-hand side of Equation 5.20 (for the conditions indicated in the caption) is also depicted in Figure 5.40. Since the pulse maximum occurs at $s = 0$, the left-hand side of (5.20) must be negative at this point (positive polarity pulses are considered). This is satisfied if the pulse amplitude is above the intersection voltage of Figure 5.40. However, this is not enough to obtain

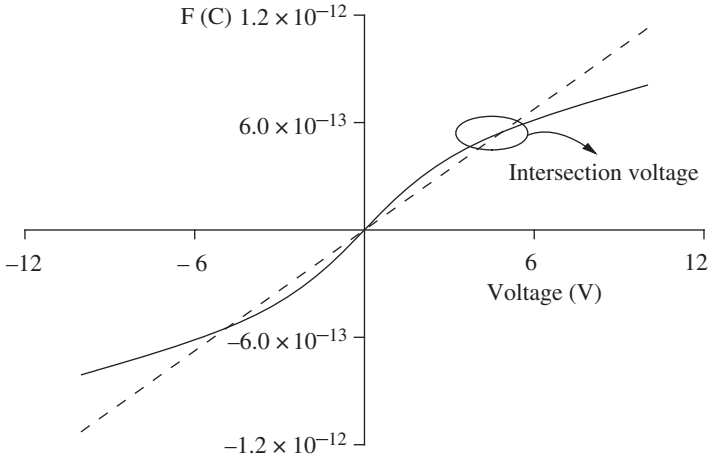

FIGURE 5.40 Representation of $F(V)$ obtained from (5.21) with $C_o = 43.5$ fF and $C_D(V) = 0.12\,\text{sech}(0.5\text{ V})$ pF (solid line). The second term of the left-hand side of equation (5.20) with $T = 3.5$ ps and $L = 108.7$ pH is also depicted (dashed line). Reprinted with permission from Ref. [87]; copyright 2001 AIP.

solutions of the form of solitons. Namely, as voltage decreases from maximum, the curvature decreases, changes polarity at the crossing point and, finally, an oscillatory behavior is found, unless the pulse amplitude takes the precise value that makes the solution vanish for $s \rightarrow \pm\infty$. In view of the previous argument and Figure 5.40, it is clear that solutions corresponding to solitary waves are only possible if there exits an intersection point between both terms of the left-hand side of Equation 5.20 above the origin. This limits the slope of the second term of the left-hand side to the range given by the asymptotic value of $F(V)$ and the derivative of $F(V)$ at the origin. This means that only solitons with per-section propagation delay T within the interval given by $[(LC_o)^{1/2}-(LC(0))^{1/2}]$ can propagate in the line. For a given T in this interval, a single solution exits, and soliton amplitude increases as T decreases. This behavior (in agreement with related literature [84]) can be deduced from Figure 5.40, where it is clearly seen that the intersection voltage increases as T approaches the lower limit of the earlier cited interval.

By numerically solving Equation 5.20, soliton solutions under arbitrary $C(V)$ characteristic can be obtained. Nevertheless, the dependence of soliton amplitude on T can be obtained without the need of solving (5.20). By multiplying Equation 5.20 by $dV(s)/ds$ and integrating in s, it follows:

$$\int_0^{\infty}\left[F(V(s))-\frac{T^2}{L}V(s)\right]\frac{dV(s)}{ds}ds=\frac{T^4}{12L}\int_0^{\infty}\frac{d^2V(s)}{ds^2}\frac{dV(s)}{ds}ds \tag{5.22}$$

The right-hand side of (5.22) can be integrated by parts and found to be equal to zero for any function satisfying $dV(s)/ds = 0$ at $s = 0$ and $s = \infty$ (these are the boundary conditions for soliton solutions). By transforming the left-hand side of (5.22) to a voltage integral we finally obtain:

$$\int_0^{V_{max}}\left[F(V)-\frac{T^2}{L}V\right]dV=0 \tag{5.23}$$

where it is assumed that $V(s\rightarrow\infty) = 0$, and $V(s = 0) = V_{max}$ is defined as the soliton amplitude. Integrating Equation 5.23, T can be isolated and compactly expressed as follows:

$$T=\frac{\sqrt{2\cdot L\cdot G(V_{max})}}{V_{max}} \tag{5.24}$$

where $G(V)$ is related to $F(V)$ by

$$G(V)=\int_0^{V}F(V')dV' \tag{5.25}$$

By means of (5.24), the dependence of per-section propagation delay on soliton amplitude, or vice versa, can be easily obtained without the need to solve any differential equation. This relationship allows one to analyze the sensitivity of propagation velocity (or T) to soliton amplitude as a function of the NLTL parameters (including the nonlineariry). This is important for the optimization of NLTL-based frequency multipliers, since a strong sensitivity of T to soliton amplitude means that the decomposition of the feeding signal into solitons proceeds faster. This improves output power, since an important reduction of device (HBV) and transmission line losses is obtained by shortening NLTL length.

5.4.2 Numerical Solutions of the Model

The details of the numerical method to solve Equation 5.20 can be found in Refs [87, 88]. The advantage of such numerical method is that it is useful regardless of the specific nonlinearity of the variable capacitance device (including the possibility to consider experimental C(V) curves to analyze soliton propagation in actual structures). In Figure 5.41, soliton waveforms with different propagation delays that correspond to the network of Figure 5.39b demonstrate that higher amplitude solitons are faster. The nonlinear capacitance has been assumed to be given by $C_D(V) = C_M \cdot \mathrm{sech}(kV)$ pF (with $C_M = 0.12$ pF and $k = 0.5\ V^{-1}$), which is a reasonable approximation to the capacitance dependence on bias for a typical HBV. Figure 5.42a depicts the interaction of two solitons obtained by numerical simulation of the network of Figure 5.39b. This figure demonstrates that solitons are stable and they preserve their identity after

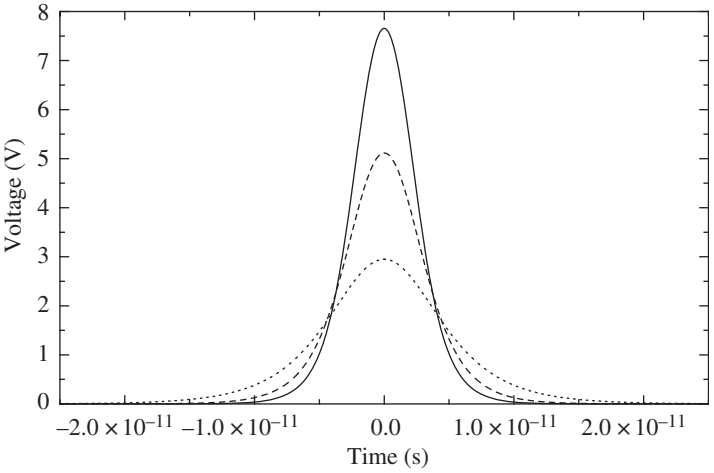

FIGURE 5.41 Soliton waveforms obtained using the approximate model for soliton propagation in NLTLs. Each curve corresponds to a different per-section propagation delay: $T = 3.5$ ps (solid line), $T = 3.75$ ps (dashed line), and $T = 4$ ps (dotted line). Model parameters indicated in Figure 5.40, which are reasonable for actual NLTLs, have been used. Reprinted with permission from Ref. [87]; copyright 2001 AIP.

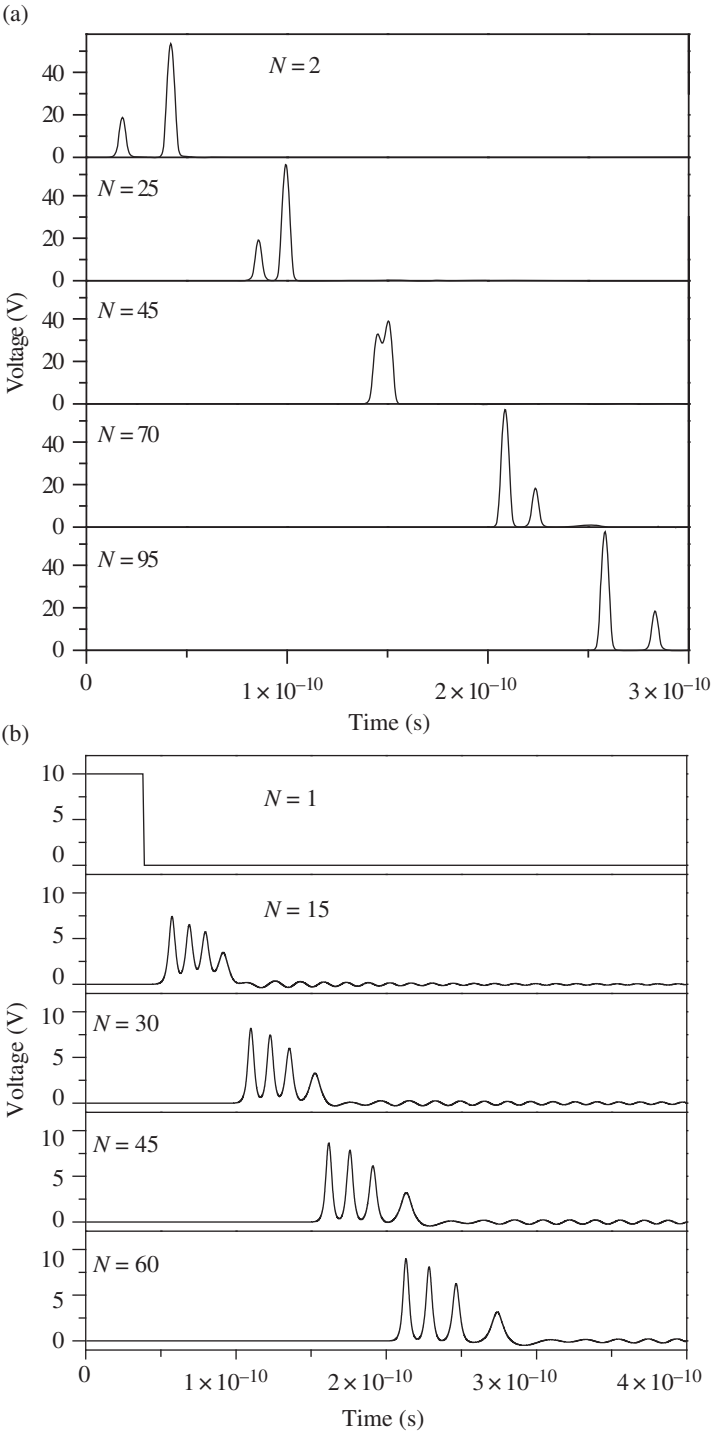

FIGURE 5.42 (a) Interaction of two solitons propagating in the same direction with different time delay ($T = 2.5$ ps for the high amplitude soliton and $T = 3$ ps for the small amplitude soliton). (b) Soliton decomposition of a 10 V square voltage pulse of 40 ps duration

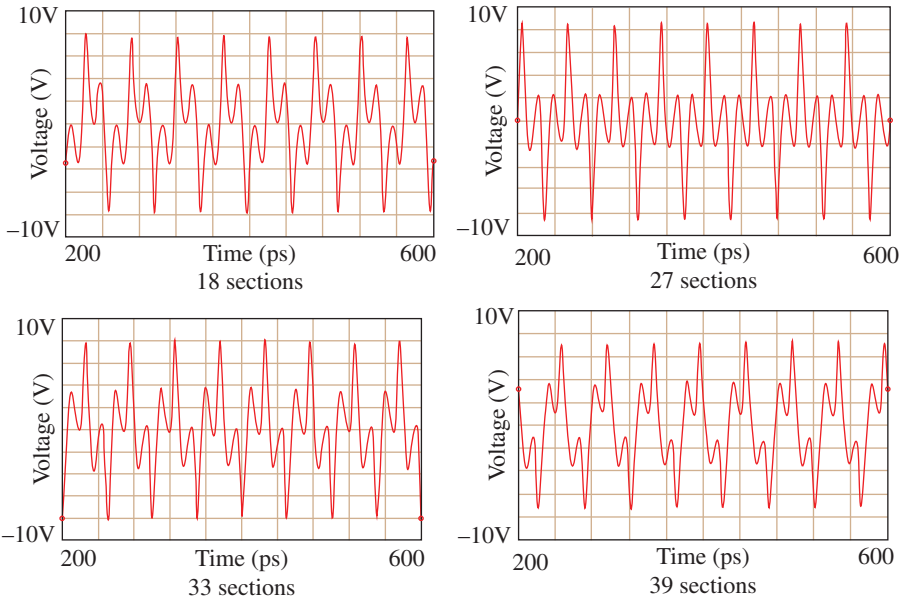

FIGURE 5.43 Voltage waveforms recorded at the output of NLTLs presenting different number of sections. Reprinted with permission from Ref. [93]; copyright 2002, Springer.

collision, as anticipated before. In Figure 5.42b, the response of the same network to a square feeding pulse indicates that the input signal progressively decomposes into solitons, and that larger amplitude solitons travel faster [91, 92].

The effects of device nonlinearity on soliton wave propagation were studied in Ref. [93], where it was pointed out that signal separation into solitons in NLTLs is enhanced by increasing device nonlinearity. Indeed, it was found in Ref. [93] that a figure of merit of the nonlinear device for harmonic generation is the area under the $C_D(V)$ curve. As this area increases, the number of sections required to optimize conversion efficiency to a given harmonic decreases, which means that soliton separation proceeds faster in structures with large $C_D(V)$ area devices. Figure 5.43 depicts the simulated waveforms obtained at the output of NLTLs with different number of sections, by considering an NLTL with $L = 108.7$ pH, $C_o = 43.5$ fF, $C_M = 0.12$ pF and $k = 0.5\ V^{-1}$, fed by a 20 GHz sinusoidal signal with 10 V amplitude. Under these conditions, the Bragg frequency is below 100 GHz. This means that significant power is only delivered to the third harmonic. The maximum dispersion

FIGURE 5.42 (*Continued*) expressed as temporal variation of voltage at several locations in the NLTL. The same NLTL parameters as in Figure 5.40 have been used. *N* indicates the section number of the line. (a) Reprinted with permission from Ref. [87]; copyright 2001 AIP; (b) Reprinted with permission from Ref. [91]; copyright 2001 Springer.

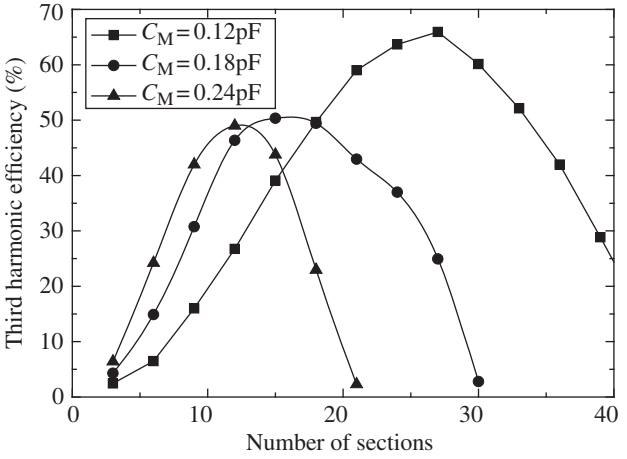

FIGURE 5.44 Effects of varying C_M on conversion efficiency, considering $k = 0.5\ V^{-1}$. Reprinted with permission from Ref. [93]; copyright 2002, Springer.

of solitons is achieved after 27 sections, where it is expected that conversion efficiency is optimized. This is corroborated in Figure 5.44, where the effects of varying C_M on conversion efficiency are depicted. Losses have not been taken into account; and for this reason, conversion efficiency is much higher than the typical values of actual structures. As can be seen, by increasing C_M the number of sections giving maximum conversion efficiency decreases. This means that conversion efficiency can be optimized with a relatively small number of sections if the equilibrium capacitance is high enough. It can be observed that for $C_M = 0.12$ pF, the maximum conversion efficiency (obtained after 27 NLTL sections) is slightly above than for the other values of the equilibrium capacitance. However, in actual NLTLs it is expected to be an important degradation of output power after 27 sections due to losses. The effects of device losses have been studied in Ref. [93]. Figure 5.45 depicts the conversion efficiency with and without losses, for two different nonlinear capacitances having the same area. The results corroborate that the area under the $C_D(V)$ curve is the key factor for efficiency optimization, and that this effect is preserved even if losses are considered.

In this section, it has been shown that NLTLs, implemented by periodically loading a host (ordinary) line with shunt-connected voltage-dependent capacitors, can support solitons. These solitons are electrical (un-modulated) pulses that propagate along the line without distortion. The study of nonlinearity in LH (actually CRLH) transmission lines was carried out in the last decade. These lines are intrinsically dispersive and, combined with nonlinear capacitances, may also support soliton propagation. However, nonlinear LH lines support solitons similar to those in optical fibers, namely, envelope (modulated) solitons, which are solutions of the nonlinear Schrödinger equation [70, 71]. In particular, it was demonstrated in [94] that, depending on the capacitance-voltage characteristic of the capacitors, a nonlinear LH transmission line

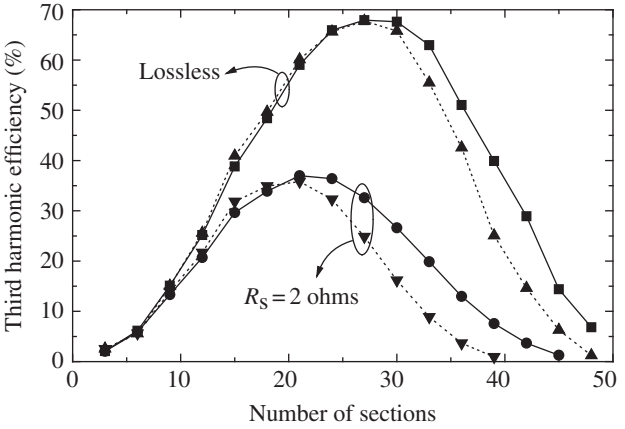

FIGURE 5.45 Effects of device losses on conversion efficiency. $C_M = 0.12$ pF, $k = 0.5$ V^{-1} (solid line); $C_M = 0.15$ pF, $k = 0.64$ V^{-1} (dotted line); the area effect is preserved when device losses are included. Reprinted with permission from Ref. [93]; copyright 2002, Springer.

can either support dark or bright[12] modulated solitons, both solutions of nonlinear Schrodinger-type equations. The analysis of soliton generation in nonlinear LH transmission lines is not straightforward, and is out of the scope of this book. Nevertheless, the author suggests references [94–103] to the interested reader on this topic.

REFERENCES

1. R. F. Pierret and G. Neudeck Editors, *The PN-Junction Diode*, Modular Series on Solid State Devices, vol. **2**, Addison Wesley, Reading, MA, 1982.
2. E. L. Kollberg and A. Rydberg, "Quantum barrier varactor for high efficiency millimeter-wave multipliers," *Electron. Lett.*, vol. **25**, pp. 1696–1698, 1989.
3. X. Melique, J. Carbonell, R. Havart, P. Mounaix, O. Vanbesien, and D. Lippens, "InGaAs/InAlAs/AlAs heterostructure barrier varactors for harmonic multiplication," *IEEE Microw, Guided Wave Lett.*, vol. **8**, pp. 254–256, 1998.
4. G. M. Rebeiz, *RF MEMS: Theory, Design, and Technology*, John Wiley, Hoboken, NJ, 2003.
5. B. Lacroix, A. Pothier, A. Crunteanu, C. Cibert, F. Dumas-Bouchiat, C. Champeaux, A. Cathérinot, and P. Blondy, "Sub-microsecond RF MEMS switched capacitors," *IEEE Trans. Microw. Theory Techn.*, vol. **55**, pp. 1314–1321, 2007.
6. B. Lakshminarayanan, D. Mercier, and G. Rebeiz, "High-reliability miniature RF-MEMS switched capacitors," *IEEE Trans. Microw. Theory Techn.*, vol. **56**, pp. 971–981, 2008.

[12] Bright solitons are pulse modulated solitons, whereas dark solitons exhibit a profile with a dip in a uniform background.

7. G. J. Papaioannou and J. Papapolymerou, "Dielectric charging mechanisms in RF-MEMS capacitive switches," *Proc. 37th European Microwave Conf.*, Munich, Germany, October 2007.
8. R. M. Young, J. D. Adam, C. R. Vale, T. T. Braggins, S. V. Krishnaswamy, C. E. Milton, D. W. Beve, L. G. Chorosinski, L.-S. Chen, D. E. Crocked, C. B. Freidhoff, S. H. Talisa, E. Capelle, R. Tranchini, J. R. Fended, J. M. Lorthioird, and A. R. Torres, "Low-loss bandpass RF filter using MEMS capacitance switches to achieve a one-octave tuning range and independently variable bandwidth," *IEEE MTT Int. Microwave Symp. Dig.*, Philadelphia, PA, June 2003, vol. **3**, pp. 1781–1784.
9. J. Papapolymerou, K. L. Lange, C. L. Goldsmith, A. Malczewski, and J. Kleber, "Reconfigurable double-stub tuners using MEMS switches for intelligent RF front-ends," *IEEE Trans. Microw. Theory Techn.*, vol. **51**, pp. 272–278, 2003.
10. S. Gevorgian, *Ferroelectrics in Microwave Devices, Circuits and Systems: Physics, Modeling, Fabrication and Measurements*, Springer-Verlag, London, 2009.
11. R. Jakoby, P. Scheele, S. Muller, and C. Weil, "Nonlinear dielectrics for tunable microwave components," *15th International Conference on Microwaves, Radar and Wireless Communications*, *MIKON*, 2004, vol. **2**, pp. 369–378.
12. P. Scheele, *Steuerbare passive Mikrowellenkomponenten auf Basis hochpermittiver ferroelektrischer Schichten*, PhD Thesis Dissertation, Technische Universität, Darmstadt, 2007.
13. J.-H. Jeon, "Effect of SrTiO3 concentration and sintering temperature on microstructure and dielectric constant of Ba(1-x)Sr(x)TiO3," *J. Eur. Ceram. Soc.*, vol. **24**, pp. 1045–1048, 2004.
14. A. Giere, P. Scheele, C. Damm, and R. Jakoby, "Optimization of uniplanar multilayer structures using nonlinear tunable dielectrics," *Proc. 35th Eur. Microw. Conf.*, Paris, France, Oct. 2005.
15. A. Giere, Y. Zheng, H. Gieser, K. Marquardt, H. Wolf, P. Scheele, and R. Jakoby, "Coating of planar Barium-Strontium-Titanate thick-film varactors to increase tunability," *Proc. 37th Eur. Microw. Conf.*, Munich, Germany, October 2007.
16. P. G. de Gennes and J. Prost, *The Physics of Liquid Crystals*, Oxford University Press, Oxford, 1995.
17. P. Collins, and M. Hird, *Introduction to Liquid Crystals: Chemistry and Physics*, Taylor & Francis, London, 1997.
18. I. W. Stewart, *The Static and Dynamic Continuum Theory of Liquid Crystals: a Mathematical Introduction*, Taylor & Francis, London, 2004.
19. I. Gil, J. García-García, J. Bonache, F. Martín, M. Sorolla, and R. Marqués, "Varactor-loaded split rings resonators for tunable notch filters at microwave frequencies," *Electron. Lett.*, vol. **40**, pp. 1347–1348, 2004.
20. I. Gil, J. Bonache, J. García-García, and F. Martín "Tunable metamaterial transmission lines based on varactor loaded split rings resonators," *IEEE Trans. Microw. Theory Techn.*, vol. **54**, pp. 2665–2674, 2006.
21. K. Aydin and E. Ozbay, "Capacitor-loaded split ring resonators as tunable metamaterial components," *J. Appl. Phys.*, vol. **101**, paper 024911, 2007.
22. J. B. Pendry, A. J. Holden, D. J. Robbins, and W. J. Stewart, "Magnetism from conductors and enhanced nonlinear phenomena," *IEEE Trans. Microw. Theory Techn.*, vol. **47**, pp. 2075–2084, 1999.

23. A. Vélez, J. Bonache, and F. Martín, "Varactor-loaded complementary split ring resonators (VLCSRR) and their application to tunable metamaterial transmission lines," *IEEE Microw. Wireless Compon. Lett.*, vol. **18**, pp. 28–30, 2008.

24. J. Bonache, M. Gil, I. Gil, J. García-García, and F. Martín, "On the electrical characteristics of complementary metamaterial resonators," *IEEE Microw. Wireless Compon. Lett.*, vol. **16**, pp. 543–545, 2006.

25. A. Vélez, F. Aznar, M. Durán-Sindreu, J. Bonache, and F. Martín, "Tunable coplanar waveguide (CPW) band-stop and band-pass filters based on open split ring resonators and open complementary split ring resonators," *IET Microw. Antennas Propag.*, vol. **5**, pp. 277–281, 2011.

26. J. S. Hong and M. J. Lancaster, *Microstrip Filters for RF/Microwave Applications*, John Wiley, New York, 2001.

27. A. Velez, F. Aznar, J. Bonache, M. C. Velázquez-Ahumada, J. Martel, and F. Martín, "Open complementary split ring resonators (OCSRRs) and their application to wideband CPW band pass filters," *IEEE Microw. Wireless Compon. Lett.*, vol. **19**, pp. 197–199, 2009.

28. A. Vélez, F. Aznar, M. Durán-Sindreu, J. Bonache, and F. Martín, "Stop-band and band-pass filters in coplanar waveguide technology implemented by means of electrically small metamaterial-inspired open resonators," *IET Microw. Antennas Propag.*, vol. **4**, pp. 712–716, 2010.

29. A. Vélez, J. Bonache, and F. Martín, "Metamaterial transmission lines with tunable phase and characteristic impedance based on complementary split ring resonators," *Microw. Opt. Technol. Lett.*, vol. **51**, pp. 1966–1970, 2009.

30. T. Hand and S. Cummer, "Characterization of tunable metamaterial elements using MEMS switches," *IEEE Antennas Wireless Propag. Lett.*, vol. **6**, pp. 401–404, 2007.

31. H. Tao, A. C. Strikwerda, K. Fan, W. J. Padilla, X. Zhang, and R. D. Averitt, "MEMS based structurally tunable metamaterials at terahertz frequencies," *J. Infrared Milli. Terahz. Waves*, vol. **32** pp. 580–595, 2011.

32. I. Gil, F. Martín, X. Rottenberg, and W. De Raedt, "Tunable stop-band filter at Q-band based on RF-MEMS metamaterials," *Electron. Lett.*, vol. **43**, p. 1153, 2007.

33. D. Bouyge, A. Crunteanu, M. Durán-Sindreu, A. Pothier, P. Blondy, J. Bonache, J. C. Orlianges, and F. Martín, "Reconfigurable split rings based on MEMS switches, and their application to tunable filters," *J. Opt.*, vol. **14**, paper 114001, 2012.

34. D Bouyge, D. Mardivirin, J. Bonache, A. Crunteanu, A. Pothier, M. Durán-Sindreu, P. Blondy, and F. Martín, "Split ring resonators (SRRs) based on micro-electro-mechanical deflectable cantilever-type rings: application to tunable stopband filters," *IEEE Microw. Wireless Compon. Lett.*, vol. **21**, pp. 243–245, 2011.

35. D. Mardivirin, A. Pothier, A. Crunteanu, B. Vialle, and P. Blondy, "Charging in dielectric less capacitive RF-MEMS switches," *IEEE Trans. Microw. Theory Techn.*, vol. **57**, pp. 231–236, 2009.

36. M. Fabert, A. Desfarges-Berthelemot, V. Kermène, A. Crunteanu, D. Bouyge, and P. Blondy, "Ytterbium-doped fibre laser Q-switched by a cantilever-type micro-mirror," *Opt. Express*, vol. **16**, pp. 22064–22071, 2008.

37. F. Martín, F. Falcone, J. Bonache, T. Lopetegi, R. Marqués, and M. Sorolla, "Miniaturized CPW stop band filters based on multiple tuned split ring resonators," *IEEE Microw. Wireless Compon. Lett.*, vol. **13**, pp. 511–513, 2003.

38. J.-S. Hong and M. J. Lancaster, "Couplings of microstrip square open-loop resonators for cross-coupled planar microwave filters," *IEEE Trans. Microw. Theory Techn.*, vol. **44**, pp. 2099–2109, 1996.

39. C.-M. Tsai, S.-Y. Lee, and C.-C. Tsai, "Performance of a planar filter using a 0° feed structure," *IEEE Trans. Microw. Theory Tech.*, vol. **50**, pp. 2362–2367, 2002.

40. A. K. Tagantsev, V. O. Sherman, K. F. Astafiev, J. Venkatesh, and N. Setter, "Ferroelectric materials for microwave tunable applications," *J. Electroceram.*, vol. **11**, pp. 5–66, 2003.

41. D. Kuylenstierna, A. Vorobiev, P. Linner, and S. Gevorgian, "Ultrawide-band tunable true-time delay lines using ferroelectric varactors," *IEEE Trans. Microw. Theory Techn.*, vol. **53**, pp. 2164–2170, 2007.

42. F. A. Miranda, F. W. Van Keuls, R. R. Romanofsky, and G. Subramanyam, "Tunable microwave components for Ku- and K-band satellite communications," *Integr. Ferroelectr.*, vol. **22** (1–4), pp. 789–798, 1998.

43. E. Ozbay, K. Aydin, S. Butun, K. Kolodziejak, and D. Pawlak, "*Ferroelectric based tuneable SRR based metamaterial for microwave applications*," *Proc. of the 37th Eur. Microw. Conf.*, Munich, Germany, October 2007, pp. 497–499.

44. M. Gil, C. Damm, A. Giere, M. Sazegar, J. Bonache, R. Jakoby, and F. Martín, "Electrically tunable split-ring resonators at microwave frequencies based on Barium-Strontium Titanate thick-film," *Electron. Lett.*, vol. **45**, pp. 417–419, 2009.

45. M. Gil, C. Damm, M. Maasch, M. Sazegar, A. Giere, F. Aznar, A. Vélez, J. Bonache, R. Jakoby, and F. Martín, "Tunable sub-wavelength resonators based on Barium-Strontium-Titanate thick-film technology," *IET Microw. Antennas Propag.*, vol. **5**, pp. 316–323, 2011.

46. F. Paul, A. Giere, W. Menesklou, J. R. Binder, P. Scheele, R. Jakoby, and J. Haußelt, "Influence of Fe-F-co-doping on the dielectric properties of Ba0.6Sr0.4TiO3 thick-films," *Int. J. Mater. Res.*, vol. **99**, pp. 1119–1128, 2008.

47. M. Durán-Sindreu, C. Damm, M. Sazegar, Y. Zheng, J. Bonache, R. Jakoby, and F. Martín, "Electrically tunable composite right/left handed transmission-line based on open resonators and barium-stronium-titanate thick films," *IEEE MTT-S Int. Microw. Symp. Dig.*, Baltimore, MD, June 2011.

48. M. Duran-Sindreu, C. Damm, M. Sazegar, Y. Zheng, J. Bonache, R. Jakoby, and F. Martín, "Applications of electrically tunable composite right/left handed transmission lines based on barium-stronium-titanate thick films and open resonators," *IET Microw. Antennas Propag.*, vol. **7**, pp. 476–484, 2013.

49. C. Damm, M. Schüßler, M. Oertel, and R. Jakoby, "Compact tunable periodically LC loaded microstrip line for phase shifting applications," *IEEE MTT-S Int. Microw. Symp. Dig.*, Long Beach, CA, June 2005, pp. 2003–2005.

50. C. Damm, M. Schüßler, J. Freese, and R. Jakoby, "Artificial line phase shifter with separately tunable phase and line impedance," *36th Eur. Microw. Conf.*, Manchester, UK, September 2006, pp. 423–426.

51. A. Giere, C. Damm, P. Scheele, and R. Jakoby, "LH phase shifter using ferroelectric varactors," *IEEE Radio Wireless Symp.*, San Diego, CA, October 2006, pp. 403–406.

52. S.-H. Hwang, T. Jang, Y.-S. Bang, J.-M. Kim, Y.-K. Kim, S. Lim, and C.-W. Baek, "Tunable composite right/left-handed transmission line with positive/negative phase tunability using integrated MEMS switches," *IEEE 23rd Int. Conf. MEMS*, Wanchai, Hong Kong, January 2010, pp. 763–766.

53. S.-H. Hwang, T. Jang, J.-M. Kim, Y.-K. Kim, S. Lim, and C.-W. Baek, "MEMS-tunable composite right/left-handed (CRLH) transmission line and its application to a phase shifter," *J. Micromech. Microeng.*, vol. **21**, paper 125022, 2011.

54. S. Lim, C. Caloz, and T. Itoh, "Electronically-controlled metamaterial based transmission line as a continuous-scanning leaky-wave antenna," *IEEE MTT-S Int. Microw. Symp. Dig.*, Fort-Worth, TX, June 2004, vol. **1**, pp. 313–316.

55. S. Lim, C. Caloz, and T. Itoh, "Metamaterial-based electronically controlled transmission-line structure as a novel leaky-wave antenna with tunable radiation angle and beamwidth," *IEEE Trans. Microw. Theory Techn.*, vol. **53**, pp. 161–173, 2005.

56. T. Kim, L. Vietzorreck, "Investigation of smart antennas using RF-MEMS based tunable CRLH-transmission lines," *Int. Conf. Electromag. Adv. Appl.*, Cape Town, South Africa, September 2012, pp. 266–267.

57. C. Damm, M. Maasch, R. Gonzalo, and R. Jakoby, "Tunable composite right/left-handed leaky wave antenna based on a rectangular waveguide using liquid crystals," *IEEE MTT-S Int. Microw. Symp. Dig.*, Anaheim, CA, May 2010, pp. 13–16.

58. M. Roig, M. Maasch, C. Damm, O. Hamza-Karabey, and R. Jakoby, "Liquid crystal based tunable composite right/left-handed leaky-wave antenna for ka-band applications," *43rd Eur. Microw. Conf.*, Nuremberg, Germany, October 2013, pp. 759–762.

59. F. Goelden, A. Gaebler, S. Mueller, A. Lapanik, W. Haase, and R. Jakoby, "Liquid-crystal varactors with fast switching times for microwave applications," *Electron. Lett.*, vol. **44**, pp. 480–481, 2008.

60. C. Damm, J. Freese, M. Schüßler, and R. Jakoby, "Electrically controllable artificial transmission line transformer for matching purposes," *IEEE Trans. Microw. Theory Techn.*, vol. **55**, pp. 1348–1354, 2007.

61. I. Vendik, D. Kholodnyak, P. Kapitanova, M.A. Hein, S. Humbla, R. Perrone, and J. Mueller, "Tunable dual-band microwave devices based on a combination of left/right-handed transmission lines," *38th Eur. Microw. Conf.*, Amsterdam, The Netherlands, October 2008, pp. 273–276.

62. A. S. Mohra and O. F. Siddiqui, "Tunable bandpass filter based on capacitor-loaded metamaterial lines," *Electron. Lett.*, vol. **45**, pp. 470–472, 2009.

63. A. L. Borja, J. Carbonell, J. D. Martinez, V. E. Boria, and D. Lippens, "A controllable bandwidth filter using varactor-loaded metamaterial-inspired transmission lines," *IEEE Antennas Wireless Propag. Lett.*, vol. **10**, pp. 1575–1578, 2011.

64. M. Morata, I. Gil, and R. Fernández-García, "Modeling tunable band-pass filters based on RF-MEMS metamaterials," *Int. J. Numer. Model. Electron. Networks, Devices Field*, vol. **24**, pp. 583–589, 2011.

65. I. Gil, M. Morata, R. Fernández-García, X. Rottenberg, and W. De Raedt, "Reconfigurable RF-MEMS metamaterials filters," *Prog. Electromag. Res. Symp. Proc.*, Marrakesh, Morocco, March 2011, pp. 1239–1242.

66. B. K. Kim and B. Lee, "Tunable bandpass filter with varactors based on the CRLH-TL metamaterial structure," *J. Electromag. Eng. Sci.*, vol. **13**, pp. 245–250, 2013.

67. M. G. Case, *Nonlinear Transmission Lines for Picosecond Pulse, Impulse and Millimeter-Wave Harmonic Generation*, PhD dissertation, University of California, Santa Barbara, July 1993.

68. A. C. Scott, F. Y. E. Chu, and D. W. McLaughlin, "The soliton: a new concept in applied science," *Proc. IEEE*, vol. **61**, pp. 1443–1483, 1973.

69. J. S. Russell, "*Report on Waves*," *Rep. 14th Meet. British Assoc. Adv. Sci.*, York, UK, September 1844, pp. 311–390.

70. P. J. Olver and D. H. Sattinger, *Solitons in Physics, Mathematics, and Nonlinear Optics*, Springer-Verlag, New York, 1990.

71. J. R. Tailor, *Optical Solitons—Theory and Experiment*, Cambridge University Press, Cambridge, 1992.

72. M. Remoissenet, *Waves Called Solitons: Concepts and Experiments*, Springer-Verlag, Berlin, Germany 1994.

73. M. J. W. Rodwell, M. Kamegawa, R. Yu, M. Case, E. Carman, and K. Giboney, "GaAs nonlinear transmission lines for picosecond pulse generation and millimeter-wave sampling," *IEEE Trans. Microw. Theory Techn.*, vol. **39**, pp. 1194–1204, 1991.

74. E. Carman, M. Case, M. Kamegawa, R. Yu, K. Giboney, and M. J. W. Rodwell, "V-band and W-band broad-band, monolithic distributed frequency multipliers," *IEEE Microw. Guided Wave Lett.*, vol. **2**, pp. 253–254, 1992.

75. H. Shi, W. M. Chang, C. W. Domier, N. C. Luhman, L. B. Sjogren, and H. L. Liu, "Novel concepts for improved transmission line performance," *IEEE Trans. Microw. Theory Techn.*, vol. **43**, pp. 780–789, 1995.

76. I. Ryjenkova, V. Mezentsev, S. Musher, S. Turitsyn, R. Hülsewede, and D. Jäger, "Millimeter wave generation on nonlinear transmission lines," *Ann. Telecommun.*, vol. **52**, pp. 134–139, 1997.

77. J. R. Thorpe, P. Steenson, and R. Miles, "Non-linear transmission lines for millimeter-wave frequency multiplier applications," *Proc. IEEE Sixth Int. Conf. on Terahertz Electron.*, Leeds, UK, 1998, p. 54.

78. M. Li and R.G. Harrison, "A fully distributed heterostructure barrier varactor nonlinear transmission line frequency tripler," *IEEE MTT-S Int. Microw. Symp. Dig.*, Baltimore, MD, June 1998, pp. 1639–1643.

79. E. Lheurette, M. Fernández, X. Melique, P. Mounaix, O. Vanbésien and D. Lippens, "Non linear transmission line quintupler loaded by heterostructure barrier varactors," *Proc. Eur. Microw. Conf.*, Munich, Germany. October 1999.

80. L. Dillner, M. Ingvarson, E. Kollberg, and J. Stake, "Heterostructure barrier varactor multipliers," *Proc. Eur. GaAs Conf.*, Paris, October 2000.

81. X. Melique, A. Maestrini, E. Lheurette, P. Mounaix, M. Favreau, O. Vanbesien, J. M. Goutoule, G. Beaudin, T. Nahri, and D. Lippens, "12% efficiency and 9.5 dBm output power from InP-based heterostructure barrier varactor triplers at 250 GHz," *IEEE MTT-S Int. Microwave Symp. Dig.*, Anaheim, CA, June 1999, vol. **1**, pp. 123–126.

82. E. Carman, K. Giboney, M. Case, M. Kamegawa, R. Yu, K. Abe, M. J. W. Rodwell, and J. Franklin, "28-39 GHz distributed harmonic generation on a soliton nonlinear transmission line," *IEEE Microw. Guided Wave Lett.*, vol. **1**, pp. 28–31, 1991.

83. M. M. Turner, G. Branch, and P. W. Smith, "Methods of theoretical analysis and computer modeling of the shaping of electrical pulses by nonlinear transmission lines and lumped-element delay lines," *IEEE Trans. Electron. Dev.*, vol. **38**, pp. 819–816, 1991.

84. R. Hirota and K. Suzuki, "Theoretical and experimental studies of lattice solitons in nonlinear lumped networks," *Proc. IEEE*, vol. **61**, pp. 1483–1491, 1973.

85. M. Toda, "Nonlinear lattice and soliton theory," *IEEE Trans. Circuits Syst.*, vol. **30**, pp. 542–554, 1983.

86. D. J. Korteweg and G. de Vries, "On the change of form of long waves advancing in a rectangular canal, and on a new type of long stationary waves," *Phil. Mag.*, vol. **39**, pp. 422–443, 1895.
87. F. Martín and X. Oriols "A simple model to study soliton wave propagation in periodically loaded nonlinear transmission lines," *Appl. Phys. Lett.*, vol. **78**, pp. 2802–2804, 2001.
88. X. Oriols and F. Martín "Analytical solitons in nonlinear transmission lines loaded with heterostructure barrier varactors," *J. Appl. Phys.*, vol. **90**, pp. 2595–2600, 2001.
89. E. Afshari and A. Hajimiri, "Nonlinear transmission lines for pulse shaping in silicon," *IEEE J. Solid-State Circuits*, vol. **40**, pp. 744–752, 2005.
90. X. Wang and R. J. Hwu, "Theoretical analysis and FDTD simulation of GaAs nonlinear transmission lines," *IEEE Trans. Microw. Theory Techn.*, vol. **47**, pp. 1083–1091, 1999.
91. F. Martín and X. Oriols "Understanding soliton wave propagation in nonlinear transmission lines for millimeter wave multiplication," *Int. J. Infrared. Milli. Waves*, vol. **22**, pp. 85–92, 2001.
92. F. Martín and X. Oriols "Effects of line parameters on soliton-like propagation in nonlinear transmission lines: application to the optimization of frequency triplers," *Int. J. Infrared Milli. Waves*, vol. **22**, pp. 225–235, 2001.
93. F. Martín, X. Oriols, J. A. Gil, and J. García-García, "Optimization of nonlinear transmission lines for harmonic generation: the role of the capacitance voltage characteristic and the area effect," *Int. J. Infrared Milli. Waves*, vol. **23**, pp. 95–103, 2002.
94. S. Gupta and C. Caloz, "Dark and bright solitons in left-handed nonlinear transmission line metamaterials," *IEEE MTT-S Int. Microw. Symp.*, Honolulu, HI, June 2007.
95. C. Caloz, I.-H. Lin, and T. Itoh, "Characteristics and potential applications of nonlinear left handed transmission lines," *Microw. Opt. Technol. Lett.*, vol. **40**, pp. 471–473, 2004.
96. A. B. Kozyrev and D. W. van der Weide, "Nonlinear transmission lines in left-handed media," *IEEE MTT-S Int. Microw. Symp.*, Fort Worth, TX, June 2004.
97. A. B. Kozyrev and D. W. van der Weide "Nonlinear wave propagation phenomena in left-handed transmission-line media," *IEEE Trans. Microw. Theory Techn.*, vol. **53**, pp. 238–245, 2005.
98. K. Narahara, T. Nakamichi, T. Suemitsu, T. Otsuji, and E. Sano, "Development of solitons in composite right- and left-handed transmission lines periodically loaded with Schottky varactors," *J. Appl. Phys.*, vol. **102**, pp. 024501–024504, 2007.
99. B. K. Alexander, and D. W. Van Der Weide, "Trains of envelope solitons in nonlinear left-handed transmission line media," *Appl. Phys. Lett.*, vol. **91**, pp. 254111–254113, 2007.
100. A. B. Kozyrev, and D. W. Van Der Weide, "Nonlinear left-handed transmission line metamaterials," *J. Phys. D: Appl. Phys.*, vol. **41**, pp. 173001–173010, 2008.
101. F. G. Gharakhili, M. Shahabadi, and M. Hakkak, "Bright and dark soliton generation in a left-handed nonlinear transmission line with series nonlinear capacitors," *Prog. Electromag. Res.*, vol. **96**, pp. 237–249, 2009.
102. Z. Wang, Y. Feng, B. Zhu, J. Zhao, and T. Jiang, "Schrödinger solitons and harmonic generation in short left-handed nonlinear transmission line metamaterial," *Proc. Asia Pacif. Microw. Conf.*, Singapore, December. 2009, pp. 1246–1249.
103. A. B. Kozyrev and D. W. van der Weide, "Nonlinear left-handed metamaterials," in *Metamaterials*, X.-Y. Jiang, Ed. InTech, May 2012.